

Bioelastic state recovery for haptic sensory substitution

<https://doi.org/10.1038/s41586-024-08155-9>

Received: 12 October 2023

Accepted: 4 October 2024

Published online: 06 November 2024

 Check for updates

Matthew T. Flavin^{1,2,21}, Kyoung-Ho Ha^{2,21}, Zengrong Guo^{3,21}, Shupeng Li^{4,21}, Jin-Tae Kim^{5,21}, Tara Saxena⁴, Dimitrios Simatos², Fatimah Al-Najjar⁶, Yuxuan Mao^{4,7}, Shishir Bandapalli⁴, Chengye Fan⁴, Dongjun Bai^{8,9,10}, Zhuang Zhang³, Yanlin Zhang³, Eunhye Flavin¹¹, Kenneth E. Madsen^{2,12}, Yi Huang³, Luoqian Emu³, Jingyang Zhao³, Jae-Young Yoo^{2,13}, Minsu Park¹⁴, Jaeho Shin^{2,15}, Aaron G. Huang¹⁴, Hee-Sup Shin², J. Edward Colgate⁴, Yonggang Huang^{4,16,17}, Zhaoqian Xie^{8,9,10}, Hanqing Jiang^{3,18,19} & John A. Rogers^{2,4,6,17,20}

The rich set of mechanoreceptors found in human skin^{1,2} offers a versatile engineering interface for transmitting information and eliciting perceptions^{3,4}, potentially serving a broad range of applications in patient care⁵ and other important industries^{6,7}. Targeted multisensory engagement of these afferent units, however, faces persistent challenges, especially for wearable, programmable systems that need to operate adaptively across the body^{8–11}. Here we present a miniaturized electromechanical structure that, when combined with skin as an elastic, energy-storing element, supports bistable, self-sensing modes of deformation. Targeting specific classes of mechanoreceptors as the basis for distinct, programmed sensory responses, this haptic unit can deliver both dynamic and static stimuli, directed as either normal or shear forces. Systematic experimental and theoretical studies establish foundational principles and practical criteria for low-energy operation across natural anatomical variations in the mechanical properties of human skin. A wireless, skin-conformable haptic interface, integrating an array of these bistable transducers, serves as a high-density channel capable of rendering input from smartphone-based 3D scanning and inertial sensors. Demonstrations of this system include sensory substitution designed to improve the quality of life for patients with visual and proprioceptive impairments.

Human skin has a rich composition of afferent neurons. During physical interaction with the skin, cutaneous mechanoreceptors (illustrated in Fig. 1a) elicit activity in these neurons and serve as the basis for the identification and localization of objects^{3,4}. An exciting recent direction in bioelectronics involves the development of systems that can engage these afferents in a fast, programmable manner^{8–11}.

In contrast with other peripheral nerves, somatosensory afferents can be selectively and noninvasively activated through direct interaction with the surface of the skin. As suggested by the emergence of systems for virtual and augmented reality, capabilities for fast, programmable manipulation of human sensory perception have wide-ranging applications in social media, gaming and

entertainment^{6,7}. Particularly compelling opportunities also exist in therapeutic biomedical systems that apply these somatosensory interfaces towards substituting and augmenting missing sensory capabilities⁵.

Reaching the full potential of these applications will require the engagement of both rapidly and slowly adapting (RA and SA, respectively) mechanoreceptors^{1,2} (Fig. 1a,b). These specialized cells, by coordinating with each other^{12,13} and with natural mechanical structures distributed throughout the skin^{14,15}, mediate the perceptual and emotional qualities of touch¹⁶. This paper introduces concepts of engineering science that enable targeting of the mechanical response profiles associated with these receptors through a wireless, real-time

¹School of Electrical and Computer Engineering, Georgia Institute of Technology, Atlanta, GA, USA. ²Querrey Simpson Institute for Bioelectronics, Northwestern University, Evanston, IL, USA.

³School of Engineering, Westlake University, Hangzhou, China. ⁴Department of Mechanical Engineering, Northwestern University, Evanston, IL, USA. ⁵Department of Mechanical Engineering, Pohang University of Science and Technology, Pohang, Republic of Korea. ⁶Department of Biomedical Engineering, Northwestern University, Evanston, IL, USA. ⁷Institute of Biomedical

Manufacturing and Life Quality Engineering, State Key Laboratory of Mechanical System and Vibration, School of Mechanical Engineering, Shanghai Jiao Tong University, Shanghai, China.

⁸State Key Laboratory of Structural Analysis, Optimization and CAE Software for Industrial Equipment, Dalian University of Technology, Dalian, China. ⁹Department of Engineering Mechanics, Dalian University of Technology, Dalian, China. ¹⁰DUT-BSU Joint Institute, Dalian University of Technology, Dalian, China. ¹¹Center for Education Integrating Science, Mathematics, and Computing, Georgia Institute of Technology, Atlanta, GA, USA. ¹²Department of Chemistry, University of Illinois Urbana-Champaign, Urbana, IL, USA. ¹³Department of Semiconductor Convergence Engineering, Sungkyunkwan University, Suwon, Republic of Korea. ¹⁴Department of Polymer Science and Engineering, Dankook University, Yongin, Republic of Korea. ¹⁵Molecular Recognition Research Center, Korea Institute of Science and Technology, Seoul, Republic of Korea. ¹⁶Department of Civil & Environmental Engineering, Northwestern University, Evanston, IL, USA. ¹⁷Department of Materials Science & Engineering, Northwestern University, Evanston, IL, USA. ¹⁸Westlake Institute for Advanced Study, Hangzhou, China. ¹⁹Research Center for Industries of the Future and School of Engineering, Westlake University, Hangzhou, China. ²⁰Department of Neurological Surgery, Feinberg School of Medicine, Northwestern University, Chicago, IL, USA. ²¹These authors contributed equally: Matthew T. Flavin, Kyoung-Ho Ha, Zengrong Guo, Shupeng Li, Jin-Tae Kim. [✉]e-mail: y-huang@northwestern.edu; zxie@dlut.edu.cn; hanqing.jiang@westlake.edu.cn; jrogers@northwestern.edu

Article

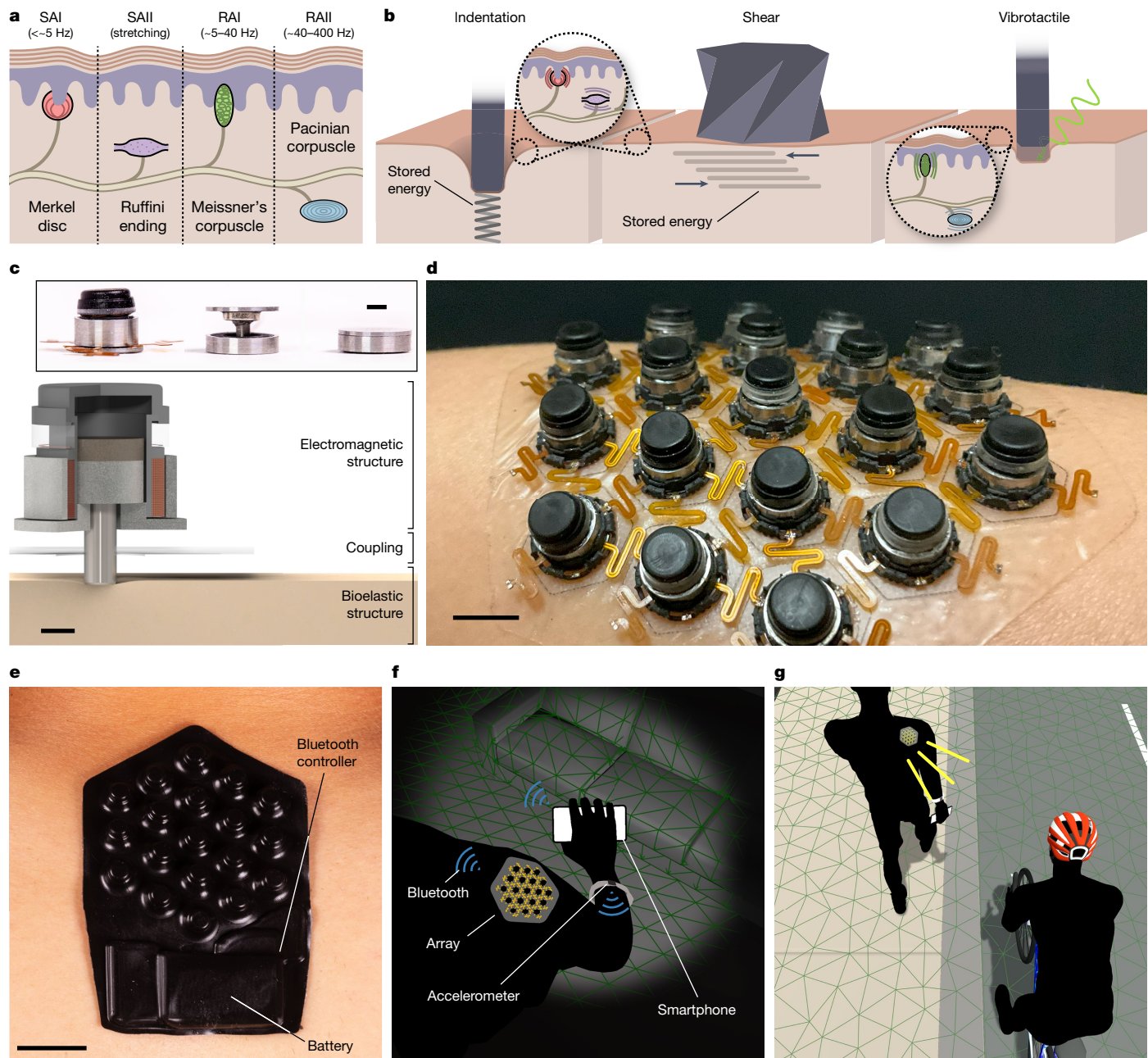


Fig. 1 | Multisensory feedback with a battery-powered array of biointegrated, bistable transducers. **a**, Diagram of skin mechanoreceptors and their frequency responses. **b**, Modes of haptic actuation, illustrating targeted mechanoreceptors. **c**, Disassembled view of the bistable transducer, featuring skin as an integral mechanical component. The inset shows a photograph of the original transducer (left) next to a miniaturized design (relaxed and compressed states shown in the middle and right, respectively). Scale bars,

2 mm. **d**, Photograph of the transducer array mounted on the shoulder. Scale bar, 7 mm. **e**, Photograph of the encapsulated interface mounted on the neck. Scale bar, 2 cm. **f**, An example of sensory substitution, with a system incorporating an array of transducers, accelerometers and 3D scanning (smartphone). Each of these components is connected to each other using the Bluetooth Low Energy protocol. **g**, An example of sensory augmentation, with a system applied to detect objects outside the field of vision of the user.

interface. Figure 1b illustrates the transmission of indentation, shear and vibrotactile stimuli through different contacting elements that include kirigami structures and cylindrical probes. The diversity in modes of engagement, density of power delivery and efficiency in operation of our small-scale mechanical transducers represent key, enabling advances over alternative electrostatic^{11,17,18}, pneumatic^{19–22} and electromagnetic^{9,10,23–27} approaches.

The foundational concept of this transducer, illustrated in Fig. 1c, is the integration of skin as a central mechanical component, yielding a bistable mechanism that recovers energy stored under compressive loading. Detailed biomechanical studies establish principles for further

miniaturization, as shown in the inset to Fig. 1c. Inductance-based self-sensing operations also lead to greater efficiency as part of a closed-loop control strategy. These features make it possible to assemble flexible, lightweight, interconnected arrays, as pictured in Fig. 1d,e, with functional diversities that greatly exceed previous reports^{9,27}. In demonstrations of this untethered, skin-conformable array as a haptic interface for sensory substitution (examples shown in Fig. 1f,g), smartphone-based sensory cues derived from 3D scanning and inertial measurements yield perceptions that improve performance in models of visual and proprioceptive sensory impairments.

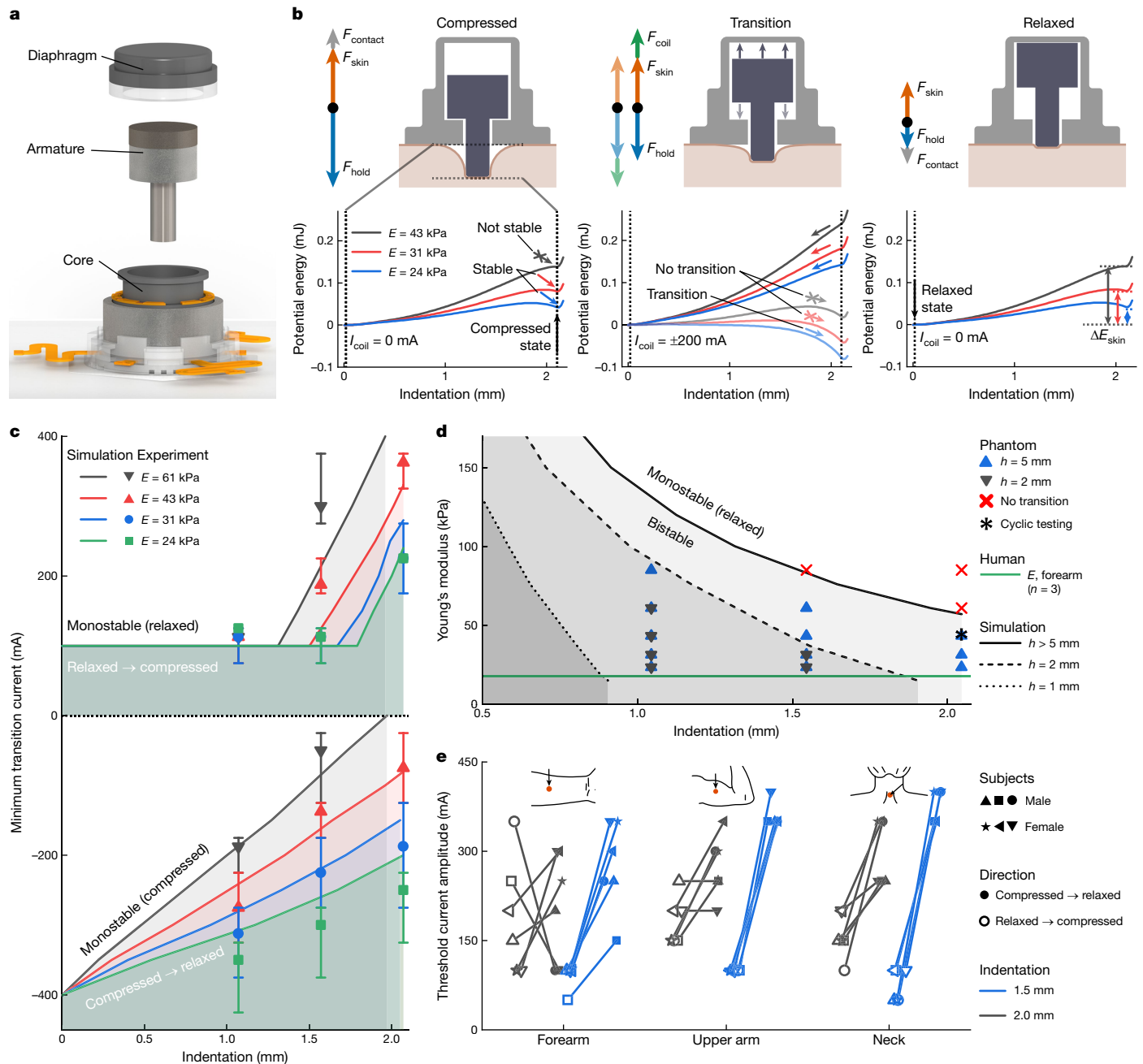


Fig. 2 | Mechanical features of the transducer and the role of skin in maintaining bistability. **a**, Disassembled view of the bistable transducer, illustrating key mechanical components. **b**, Schematic illustrations, free-body diagrams and potential energy associated with each state and transition (F_{skin} , the reactive force of skin; F_{hold} , the holding force from the permanent magnet; F_{contact} , the force of contact between the armature and opposing surfaces; F_{coil} , the force applied by driving the coil with current; ΔE_{skin} , energy stored as skin compression). The solid and faint traces correspond to operations with negative and positive (or zero) currents, respectively. The potential energy is calculated from simulations as the integral of force over the indentation depth. **c**, The minimum applied current required to overcome the energy barrier between each state plotted against the total indentation depth for a range of Young's moduli, E . The shaded regions correspond to the boundaries of

bistability, outside which only one state is attainable (monostable, compressed or relaxed). The symbols correspond to experimental evaluation of the threshold on skin phantoms (bars show min–max; $n = 4$). **d**, Phase diagram for $I_{\text{coil}} \rightarrow \infty$ showing regions across the parameter space of skin modulus and indentation depth for successful bistability. These regions are plotted for different layer thicknesses, h . The points correspond to experimental results from skin phantoms, for which transitions are observed for $I_{\text{coil}} \leq 500$ mA. The asterisk indicates conditions ($h = 5$ mm) at which successful transitions occurred over 120,000 consecutive cycles in a 96-h period. **e**, Mechanical bistability evaluation on three skin locations in $n = 6$ healthy individuals (3 male, 3 female, ages 20–36 years; locations indicated on the horizontal axis). The indentation depth was adjusted using three harness variants.

Bioelastic, bistable operation

The ability to store and release mechanical energy in skin arises from three mechanically distinct components—the core, armature and diaphragm (Fig. 2a and Extended Data Fig. 1). The core contains an

electromagnetic coil embedded in a soft ferromagnetic (iron–cobalt) cylinder, which serves to focus magnetic fields along its central longitudinal axis and to reduce interference between closely spaced units (Extended Data Fig. 3c). Iron–cobalt also appears as part of the armature assembly, along with a neodymium permanent magnet and titanium rod.

Article

This rod interfaces with the skin as a linear shaft that translates through the core. An elastomeric diaphragm, a composite of polydimethylsiloxane (PDMS) and magnetic nanopowder (MNP), encloses the top of the structure. Each transducer couples to the skin through an adhesive layer with rigid, twist-locking harnesses whose heights can be adjusted to change the effective indentation depth of the armature (Extended Data Figs. 1 and 2). To reduce mechanical mismatch between the rigid actuators and the soft, elastomeric adhesive layer, the bonding areas of the harnesses are reinforced with composites of patterned fibreglass mesh.

The core, armature and diaphragm, on mechanical coupling with the skin, form a bistable mechanism, in which energy stored by compressing the skin is returned following transition to relaxed conditions. In the compressed state (illustrated in Fig. 2b and Supplementary Video 1), the magnetic field imposed by the permanent magnet, channelled through the armature, magnetizes the soft ferromagnetic core. The strong attraction induced between these elements exceeds the reactive force imposed by the skin, thereby maintaining compression without current applied at the coil. From this state, driving the coil with opposite polarity to the permanent magnet substantially weakens its effect on the core, thus allowing the skin to push the armature into the relaxed state.

In the relaxed state (illustrated in Fig. 2b), the elasticity of the skin, along with a slight attraction to the PDMS–MNP diaphragm, prevents the armature from reverting without applied current. From the relaxed state, driving the coil in alignment with the permanent magnet polarizes the armature and core, overcomes the compressive force of the skin and drives the armature to transition back into the compressed state. Using this bistable operation, the power unit dissipates energy to transition between each state but not to persistently remain in any state.

Mechanical integration of the skin and bistable operation of the transducer requires that: (1) local energetic minima exist at the compressed and relaxed states and (2) polarization of the coil transiently induces transitions between these states (see potential energy graphs of Fig. 2b). Across a range of mechanical properties and input parameters, systematically examined through numerical modelling (Extended Data Fig. 3) and direct evaluation on skin phantoms (Supplementary Fig. 1), the shaded regions in Fig. 2d and Fig. 2c bound conditions satisfying the first and second criteria, respectively. Figure 2c shows that a successful transition from relaxed to compressed requires larger driving currents for stiffer skin, whereas the transition from compressed to relaxed follows the opposite trend. Furthermore, transitions were highly consistent (asterisk in Fig. 2d). As shown in Fig. 2e, the transducer operates successfully across three skin locations on six human participants with applied currents of at most 400 mA (see Extended Data Fig. 4 and Supplementary Fig. 2 for more skin locations).

Figure 2e and Supplementary Tables 1 and 2 show that each skin location recovers varying amounts of energy, consistent with the range of skin mechanical properties recorded in Extended Data Fig. 4. Considering that the transducer requires 1.17 J of input work to transition to the relaxed state without skin being present, the transducer saves between 742 and 1,169 mJ from the contribution of skin in the locations reported in Supplementary Tables 1 and 2 for 2-mm indentations. To accommodate these variations, the transducers feature an inductance-based self-sensing mechanism, which—as subsequently described—tailors input power on demand. Requiring only 58 mJ on average for transitions (2-mm indentation; Supplementary Tables 1 and 2), the transducers lead to linear displacements greater than 2 mm and forces of up to 1.4 N (Extended Data Fig. 4b). As outlined in Supplementary Table 3, this device, although compact and untethered, exceeds benchmark performances of alternatives based on electrostatic and electromagnetic schemes. These systematic investigations also yield principles for optimization—as shown in Extended Data Fig. 8, mechanical characterization reveals that an optimized unit of height of 2.1 mm (4.1 mm, relaxed state), operating over a narrower range of indentations, has performance matching the original design for 2-mm indentations.

Bimodal vibrotactile actuation

The mechanical structure of skin, along with its role in the bistable operation of our transducers, helps define a spring–mass system that serves as the basis for delivering vibrotactile feedback (Fig. 3a and Extended Data Fig. 3f). In the relaxed state, this spring arises from the elasticities of the skin and PDMS–MNP diaphragm, which interact with the armature on opposing ends. To allow a similar effect in the compressed state, the transducer contains an elastomeric disc layered between the core and the armature. As shown in Fig. 3a–c, applying an alternating current at sub-transition amplitude vibrates the armature, creating a small perturbation around the initial state of the transducer. Following the hysteresis curve shown in Fig. 3b, the transducer can bias its modes of vibration to the static position of either the relaxed or compressed states, depending on its history.

As shown in Fig. 3c,d, the spatiotemporal profiles of mechanical deformation, measured with 3D digital image correlation (DIC) on skin phantoms (Extended Data Fig. 5), clearly distinguish these two modes of vibration. For each frequency tested, human participants ($n=12$) perceive vibrotactile stimulus in both the relaxed and compressed states with thresholds reported in Fig. 3e and Extended Data Fig. 7a,b. A larger threshold emerges for the compressed state, following the underlying trend in deformation amplitude shown in Fig. 3c,d. The thresholds reported in Fig. 3e may also be influenced by the relative engagement of SA and RA mechanoreceptors^{28,29}.

Our system aims to deliver static indentation and dynamic vibration as perceptually distinct channels of information. On this basis, Fig. 3f,g demonstrates how integrating these operations allows the transducer to deliver information at faster bit rates, given a fixed budget for power consumption. Figure 3g also indicates that bistable operation in the 0–2 bits s⁻¹ regime offers superior power consumption with respect to purely vibrational modes. The independent and simultaneous control of indentation and vibration also raises the prospect for manipulation of a broader range of sensations that incorporate mixed input from SA and RA mechanoreceptors^{28,29}.

Kirigami structures deliver shear force

Human tactile perception not only reflects the temporal pattern of mechanical stimuli but also the direction of applied forces^{14,15}. Generalizing the contact surface of the transducer beyond a simple indenting rod, Fig. 3h,i illustrates a kirigami structure that transmits the normal-directed force of the armature into tangential forces applied parallel to the surface of the skin. This Kresling-pattern-inspired^{7,30,31} structure arises from the patterning, bonding and creasing of stiff plastic panels into a thin-walled hexagonal tube (Fig. 3j). As illustrated in Extended Data Fig. 6, the split-crease design accommodates the transducer within the internal volume of the structure itself. On linear compression, as simulated in Fig. 3k (Extended Data Fig. 3), the pattern twist-buckles into a truss of supporting beams.

Assembled into two counter-rotating tiers, the design shown in Fig. 3h–j allows low-friction rotational coupling between two contacting elements adhered to the skin. The neodymium magnet within the armature, one of the adhering elements, pulls the core of the transducer towards it under its permanent magnetic field. Because the two tiers have opposite chiralities, longitudinal motion of the middle platform drives the top and bottom platforms to rotate in opposite directions. The bottom platform couples to the skin as a ring positioned concentrically around the armature. The top platform, fixed to the shaft of the armature, couples to the skin through its adhesion with the neodymium magnet of the armature. Therefore, operation of the transducer renders twisting motions in the armature and ring in opposite directions (Supplementary Video 3). These principles similarly define the operation of a miniaturized, one-tiered structure described in Extended Data Fig. 8. As with normal-force operation, these transducers maintain two stable

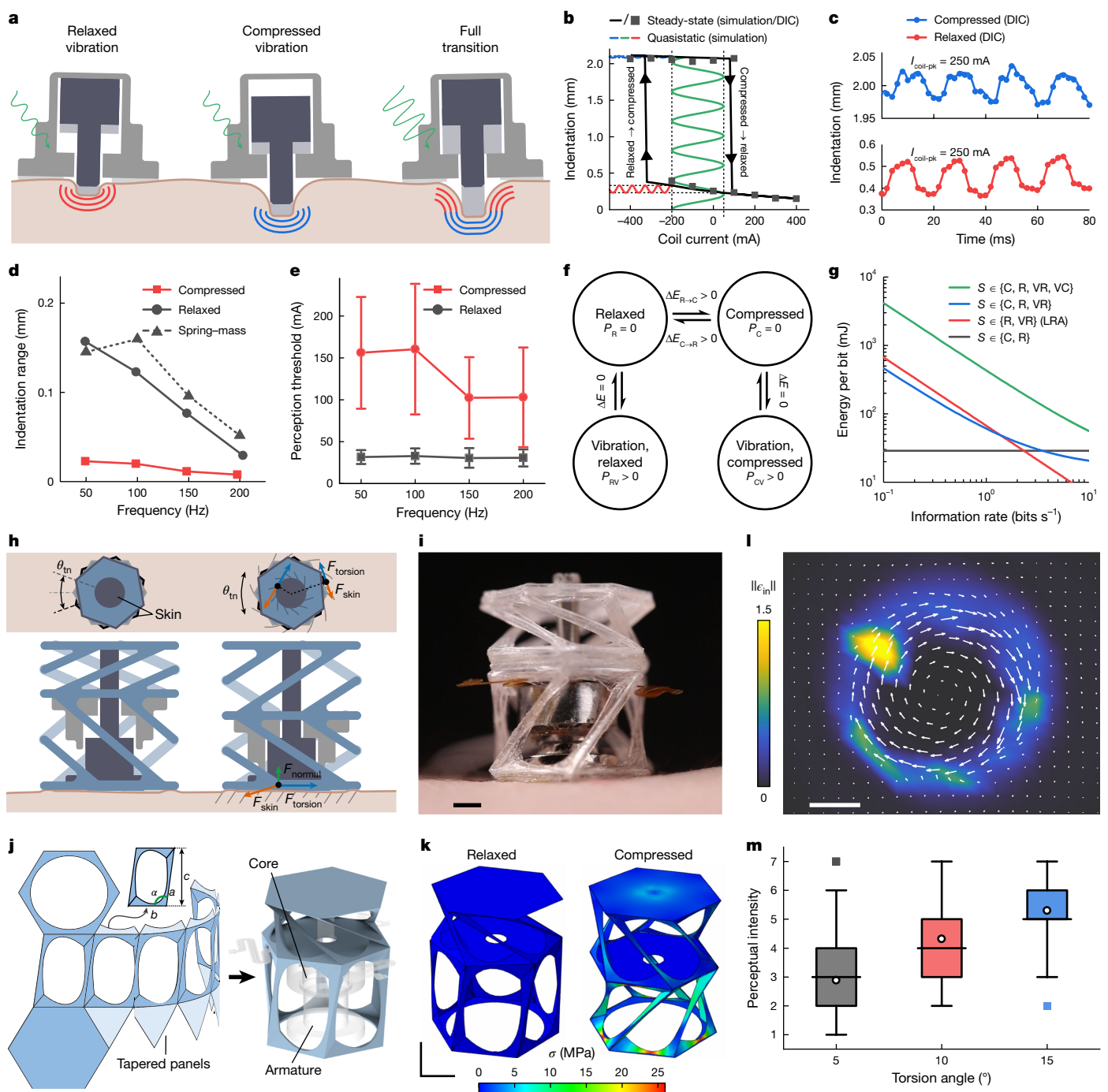


Fig. 3 | Vibrotactile and shear-force operation of the transducer.

a, Schematic illustration of the transducer in three modes of vibration. **b**, Steady-state and quasistatic behaviour of the system during scanning of coil current ($E = 43$ kPa phantom), giving rise to hysteresis. **c**, Temporal profile of deformation measured with DIC during vibration in each state ($I_{\text{coil-pk}} = 250$ mA; $f = 50$ Hz; $E = 43$ kPa phantom). **d**, Frequency profile of vibrotactile deformations (DIC and spring–mass simulation). **e**, Vibration-current amplitudes of perception thresholds ($n = 12$, 6 male, 6 female, ages 20–36 years). **f**, State diagram showing the transition energies and continuous power consumptions associated with each state. **g**, Energy cost to transmit information to the skin as a function of information rate, given different subsets of states (Methods). **h**, Schematic illustration of the torsion modality of the transducer (F_{skin} , skin reactive force; F_{torsion} , applied tangential force; F_{normal} , applied normal force; θ_{tn} , angle of torsion).

i, Photograph of the integrated kirigami structure. Scale bar, 2 mm. **j**, Assembly of the planar pattern into a 3D kirigami structure (a , b , c and α are key design parameters). **k**, Finite element analysis of stress driven by creasing within the kirigami structure (PET yield stress, 80 MPa). Scale bars, 3 mm. **l**, DIC in-plane strain on a skin phantom ($E = 31$ kPa); arrows, direction and magnitude of in-plane deformation). Scale bar, 2 mm. **m**, Perceptual intensity reported by human participants for contacting elements matching that of the integrated transducer and deformations matching DIC results ($n = 14$, 8 male, 6 female, ages 23–31 years; $P < 0.0001$, Friedman test; whiskers, 5th–95th percentiles; boxes, interquartile range; horizontal lines, medians; open circles, means; square markers, 5th–95th percentile outliers).

states balanced by the elastic force of the skin and the holding force of the permanent magnet. Also as with normal-force operation, vibratory modes are possible in either of these two states.

With the compact, efficient design reported here, the kirigami transducer generates a total rotation of up to 14° between the disc and ring elements, as measured by 3D DIC on a skin phantom ($E = 31$ kPa).

Article

Furthermore, only 0.4 mm of normal deformation is generated for this torsion angle. Figure 3*i* and Supplementary Video 4 demonstrate that the maximal tangential strain, focused on the edges of the disc, reaches more than 75%. The disc, having a smaller radius than the ring, accounts for the largest deformation. The one-tiered structure, meanwhile, yields a rotation of 7.5° and a normal deformation of 0.25 mm (Extended Data Fig. 8).

Human participants ($n = 14$), as shown in Fig. 3*m* (Extended Data Fig. 7*d–g*), report a clear increase in perceptual intensity as the angle of torsion increases from 5° to 15°. Extended Data Fig. 7*h,i* shows that participants ($n = 15$) can clearly distinguish this torsional mode from indentation with an accuracy of 97.5% (mean; 0.060% s.d.). Similarly, participants ($n = 12$) can clearly distinguish between simultaneous patterns of torsion with an overall mean accuracy of 80.6%, as evaluated in the context of a three-unit arrangement reported in Extended Data Fig. 7*j*. These outcomes support the potential of multimodal arrays, such as the one pictured in Extended Data Fig. 8*i*, and they pave the way for deeper understandings about the perception of shear forces generated from such arrays.

Self-sensing from a wireless array

Both normal and shear modes of actuation rely critically on mechanical coupling to the skin to support bistable operation. Spatial and temporal variability in the mechanical behaviour of skin, as documented in Fig. 2*e*, motivate the use of the self-sensing control strategy summarized in Fig. 4*a,b*. Through inductance-based measurements, the transducer itself can serve as a sensor for the longitudinal position of its armature (Fig. 4*c*). The circuit elements outlined in Fig. 4*b* capture the resonance frequency of each transducer and report to the controller whether it exists in the relaxed state or the compressed state (Fig. 4*d*). As the basis for a closed-loop system, self-sensing allows the transducer to recover energy stored in skin deformations, which would otherwise dissipate under mismatched transition currents.

Integrated as part of the hexagonal array described in Fig. 4*a,b*, a Bluetooth controller routes this sensor input, along with output from drivers, to 19 transducers through a layer of serpentine interconnects. The modular design of each identical transducer unit, illustrated in Extended Data Fig. 2*d*, enables flexible reconfiguration of the array while tolerating repeated mechanical bending and stretching (1,000 cycles; Supplementary Methods and Extended Data Fig. 2*h–m*). Each haptic unit is pitched at 1.3 cm, well within the reported spatial acuity of most skin areas, including the neck and forearm (5.5 mm and 2.4 mm by two-point discrimination population means, respectively)^{32,33}. Considering these principles, Extended Data Fig. 8*i* shows an array with units for both torsion and indentation that can be used as sub-pixels within these areas.

A small 500-mAh lithium-ion battery, integrated within the controlling circuit, supplies power to the entire system. In system-level demonstrations—described in the following section—the battery regularly sustains operation over 3-h intervals without losing performance. Putting aside power losses from the controller, the 500-mAh capacity of the battery would, in principle, allow the transducer to transition twice per second over 16 h, given an average input energy of 58 mJ across both transitions (derived from Supplementary Tables 1 and 2). Without closed-loop control, each transition towards compressed and each transition towards relaxed would consume 6.36 mJ and 323 mJ more energy, respectively (285% overall; average across six participants, three skin locations), to accommodate the full range of input thresholds recorded in Supplementary Tables 1 and 2. With output voltage buffered by a supercapacitor (Fig. 4*b*), the controller can transition all 19 units simultaneously and at least 29 units per second on average given 58 mJ per transition. As shown in Supplementary Video 5, the peak array temperature remains under 40 °C during characteristic conditions for the system-level demonstrations outlined in the following section.

3D scanning enables sensory substitution

Figure 4*a* illustrates the operation of a system that draws real-time information from an advanced suite of sensors offered in modern smartphones. With respect to an internal reconstruction of the surrounding environment, as visualized in Fig. 4*e*, inertial measurement units (IMUs) and light detection and ranging (LiDAR) 3D scanners track the position and orientation of the user. Our haptic device receives this sensory information over a Bluetooth connection and renders feedback to the user as replacement or augmentation of their sensory abilities. In our demonstrations, the user wears the haptic device on the back of their neck (as shown in Fig. 1*e*), which provides an intuitive frame of reference for virtual objects that follow the orientation of the body. Figure 4*f–h* illustrates how this single configuration can address three separate sensory impairments using different profiles of indentation and vibration.

The first sensory substitution system, illustrated in Fig. 4*f*, aims to help individuals with visual impairment detect obstacles in their path. As shown in Fig. 4*f*, Extended Data Fig. 9*a* and Supplementary Video 6, a smartphone held by the participant anchors six virtual detection windows to the room using LiDAR at a variable distance (2.5 m in this example) from the user. Each window sends a pattern of skin indentation to the haptic device when a physical object crosses its respective boundary at the prescribed distance. In healthy, blindfolded participants ($n = 7$), this sensory substitution system yields an accuracy of 81.8% across all participants and cues (Fig. 4*i*). As shown in Extended Data Fig. 9, participants perform best when distinguishing the horizontal position of cues. Finally, Supplementary Videos 7 and 8 provide examples of participants navigating around obstacles with this system in a hands-free configuration.

Another configuration of this system, illustrated in Fig. 4*g*, provides feedback during standing balance as a means of enhancing postural stability. As shown in Fig. 4*g*, a smartphone held against the body of the participant tracks its orientation using an IMU. These data serve feedback to the haptic device, which—analogous to a spirit level—renders a line of vibration that follows the postural angle of the user (Extended Data Fig. 9*i*). In healthy participants ($n = 10$), this sensory substitution system improves performance on the standard sharpened Romberg test. As shown in Fig. 4*j* and Extended Data Fig. 9, participants maintain their balance 20–313% longer on average under guidance from the haptic device.

Finally, Fig. 4*h* illustrates an application that aims to guide foot orientation in individuals with impaired proprioceptive control. Adverse foot positioning is often an inciting event for ankle injury^{34,35}. As shown in Fig. 4*h* and Extended Data Fig. 10*a*, the user wears an external IMU in their shoe and holds a smartphone in their hand. The smartphone uses LiDAR to track the orientation of an adjacent surface and the external IMU to track foot orientation. The haptic device receives these streams of information and renders vibration in the direction of error between the foot and surface (Extended Data Fig. 10*b*). With their eyes closed, this sensory substitution system allows healthy participants ($n = 3$) to match their foot-strike orientation to a target surface positioned at varying combinations of pitch and yaw. The magnitude of error for each participant, shown in Fig. 4*k* and Extended Data Fig. 10, is 8.82° (mean; 5.33° s.d.; $n = 172$, three participants). As demonstrated in Extended Data Fig. 10, each participant produces consistent results, even with step intervals under 1 s, suggesting that this information can be used in real time to help them adjust their motion.

Conclusions

Interfacing with the skin through an energy-recovering mechanism, the bistable, self-sensing transducer introduced here offers new operational modes and associated haptic sensations that substantially exceed the performance of other approaches. These concepts

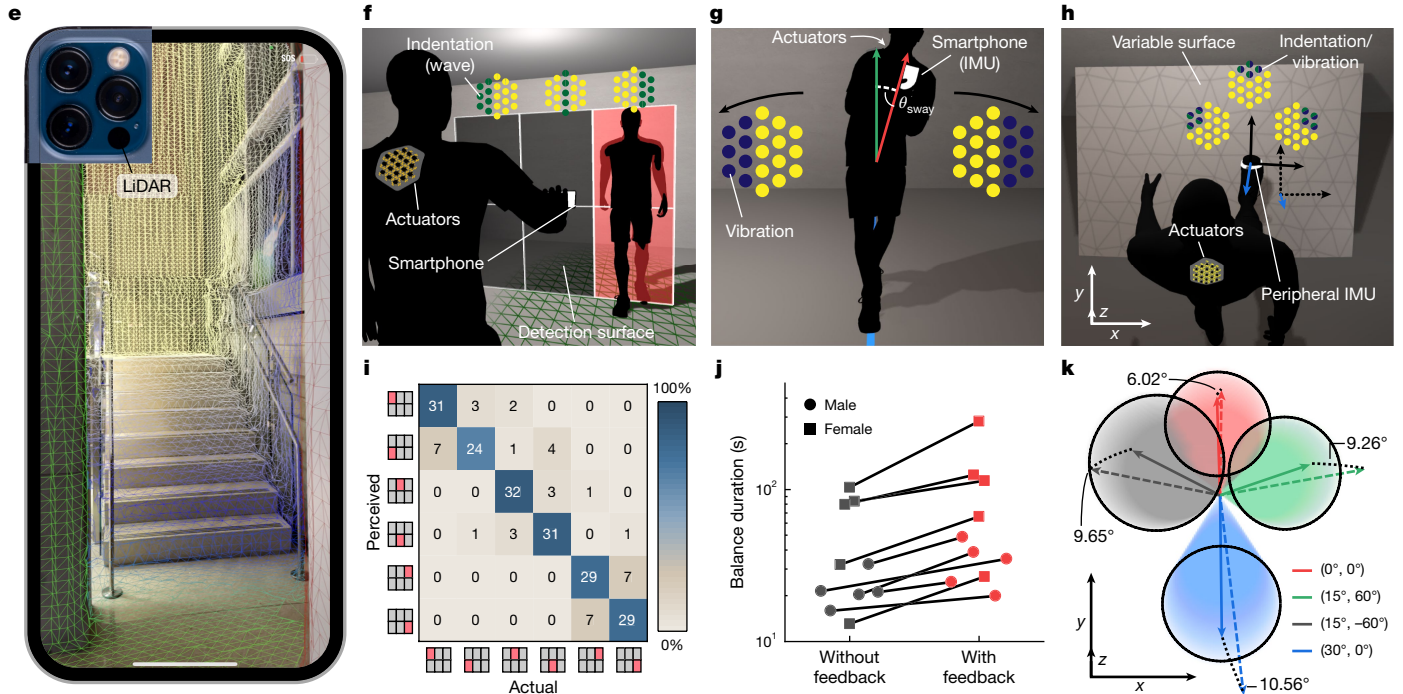
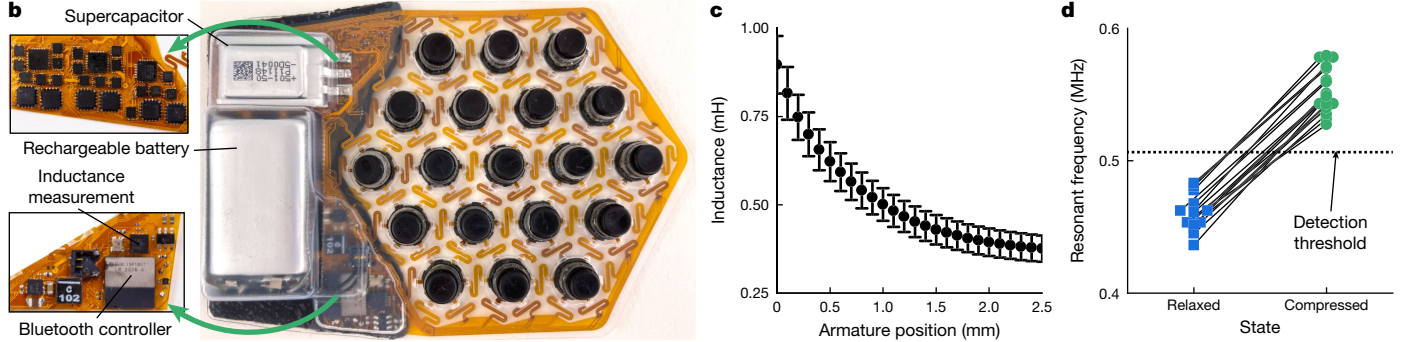
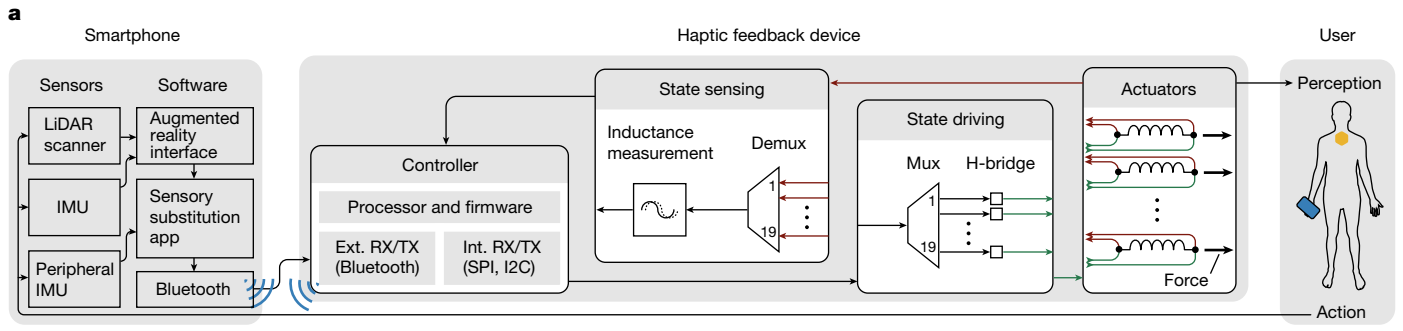


Fig. 4 | System-level implementation of an array of bistable transducers. **a**, State diagram illustrating closed-loop control system and Bluetooth communication. **b**, Photograph of transducer array integrated with driving electronics and closed-loop control system. **c**, Inductance measurement of the transducer as a function of armature position (1 kHz; $n = 4$). **d**, Resonant-frequency measurements of 19 transducers using the integrated controller. The horizontal line indicates the threshold chosen to discriminate between the relaxed and compressed states. **e**, Photograph illustrating scene reconstruction mediated by LiDAR in a smartphone. **f**, Diagram illustrating experimental setup and stimuli pattern (wave of indentation) for visual sensory substitution task. **g**, Diagram illustrating experimental setup and stimuli pattern (vibration) for balance sensory substitution task. **h**, Diagram illustrating experimental setup and stimuli pattern (vibration and indentation) for foot-strike sensory substitution task. **i**, Confusion matrix of participant performance on visual

task, with colour map indicating frequency of occurrence ($n = 7$, 4 male, 3 female, ages 19–37 years; $P = 0.0178$, Wilcoxon signed-rank test, H_0 : random selection between six choices). **j**, Participant balance duration in the sharpened Romberg task, comparing averages of repeat measures for each participant with and without feedback ($n = 10$, 5 male, 5 female, ages 20–36 years; $P = 0.00103$, repeated measures ANOVA, H_0 : no differences exist in group means). **k**, Foot-strike vectors for four surfaces presented with variations in pitch and yaw (55–60 repeat measures; $n = 3$, 2 male, 1 female, ages 21–37 years; $P < 0.001$ within each participant, Wilcoxon signed-rank test, H_0 : equal median to control). The legend lists angle combinations of (pitch, yaw) for the target surface. The solid arrows and transparent cones correspond to the mean and standard deviations of the foot unit normal vectors, respectively. The dashed arrows indicate unit normal vectors of the target surfaces.

serve as the foundation for a programmable, skin-conformable array that receives and renders patterns of multimodal mechanical stimuli. Through its ability to deliver large forces and displacements, it can reproduce cutaneous sensations associated with both SA and RA classes of mechanoreceptors. It can also blend static and dynamic deformations, addressing sensations that require coordinated and simultaneous engagement between these classes. Finally, using a compact, efficient kirigami transmission structure, it can manipulate the direction of force. These mechanosensory pathways contribute to a broad range of important human sensory perceptions, including the origin, direction and textural quality of skin contact made with its physical environment. Thus, the ability to simultaneously deliver indentation, torsion and vibration offers a strong basis for immersive haptic realism and improved intuitiveness of its applications. This multisensory operation is especially well suited for biomedical applications that require integration of complex streams of somatosensory information, such as those examined herein. In demonstrations of a wireless, skin-conformable haptic interface, smartphone-based sensory cues derived from 3D scanning and inertial measurements yield perceptions that improve performance in models of visual, vestibular and proprioceptive sensory substitution tasks.

Online content

Any methods, additional references, Nature Portfolio reporting summaries, source data, extended data, supplementary information, acknowledgements, peer review information; details of author contributions and competing interests; and statements of data and code availability are available at <https://doi.org/10.1038/s41586-024-08155-9>.

1. Bolanowski, S. J. et al. Four channels mediate the mechanical aspects of touch. *J. Acoust. Soc. Am.* **84**, 1680–1694 (1988).
2. Handler, A. & Ginty, D. D. The mechanosensory neurons of touch and their mechanisms of activation. *Nat. Rev. Neurosci.* **22**, 521–537 (2021).
3. Lederman, S. J. & Klatzky, R. L. Hand movements: a window into haptic object recognition. *Cogn. Psychol.* **19**, 342–368 (1987).
4. Lederman, S. J. & Klatzky, R. L. Haptic perception: a tutorial. *Atten. Percept. Psychophys.* **71**, 1439–1459 (2009).
5. Shull, P. B. & Damian, D. D. Haptic wearables as sensory replacement, sensory augmentation and trainer – a review. *J. Neuroeng. Rehabil.* **12**, 59 (2015).
6. Ko, S. H. & Rogers, J. Functional materials and devices for XR (VR/AR/MR) applications. *Adv. Funct. Mater.* **31**, 2106546 (2021).
7. Zhang, Z. et al. Active mechanical haptics with high-fidelity perceptions for immersive virtual reality. *Nat. Mach. Intell.* **5**, 643–655 (2023).
8. Lin, W. et al. Super-resolution wearable electrotactile rendering system. *Sci. Adv.* **8**, eabp8738 (2022).
9. Yu, X. et al. Skin-integrated wireless haptic interfaces for virtual and augmented reality. *Nature* **575**, 473–479 (2019).
10. Jung, Y. H. et al. A wireless haptic interface for programmable patterns of touch across large areas of the skin. *Nat. Electron.* **5**, 374–385 (2022).
11. Leroy, E. & Shea, H. Hydraulically amplified electrostatic taxels (HAXELs) for full body haptics. *Adv. Mater. Technol.* **8**, 2300242 (2023).
12. Turecek, J., Lehnert, B. P. & Ginty, D. D. The encoding of touch by somatotopically aligned dorsal column subdivisions. *Nature* **612**, 310–315 (2022).
13. Neubarth, N. L. et al. Meissner corpuscles and their spatially intermingled afferents underlie gentle touch perception. *Science* **368**, eabb2751 (2020).
14. Daly, C. H. Biomechanical properties of dermis. *J. Invest. Dermatol.* **79**, 17s–20s (1982).
15. Maeno, T., Kobayashi, K. & Yamazaki, N. Relationship between the structure of human finger tissue and the location of tactile receptors. *JSM Int. J. Ser. C* **41**, 94–100 (1998).
16. Klatzky, R. L. & Peck, J. Please touch: object properties that invite touch. *IEEE Trans. Haptics* **5**, 139–147 (2012).
17. Acome, E. et al. Hydraulically amplified self-healing electrostatic actuators with muscle-like performance. *Science* **359**, 61–65 (2018).
18. Grasso, G., Rosset, S. & Shea, H. Fully 3D-printed, stretchable, and conformable haptic interfaces. *Adv. Funct. Mater.* **33**, 2213821 (2023).
19. Qi, J. et al. HaptiGlove—untethered pneumatic glove for multimode haptic feedback in reality–virtuality continuum. *Adv. Sci.* **10**, 2301044 (2023).
20. Zhu, M. et al. In Proc. 2020 CHI Conference on Human Factors in Computing Systems 1–12 (Association for Computing Machinery, 2020).
21. Song, K. et al. Pneumatic actuator and flexible piezoelectric sensor for soft virtual reality glove system. *Sci. Rep.* **9**, 8988 (2019).
22. Takahashi, N., Takahashi, H. & Koike, H. In Proc. 2019 IEEE World Haptics Conference (WHC) 217–222 (IEEE, 2019).
23. Haga, Y. et al. Dynamic Braille display using SMA coil actuator and magnetic latch. *Sens. Actuators A Phys.* **119**, 316–322 (2005).
24. Karastanov, D. N., Atanassova, V. K. & Doukovska, L. A. In Proc. Third International Conference on Telecommunications and Remote Sensing 88–93 (SciTePress, 2014).
25. Vechev, V. et al. In Proc. 2019 IEEE Conference on Virtual Reality and 3D User Interfaces (VR) 312–320 (IEEE, 2019).
26. Song, E. et al. Miniaturized electromechanical devices for the characterization of the biomechanics of deep tissue. *Nat. Biomed. Eng.* **5**, 759–771 (2021).
27. Li, D. et al. Miniaturization of mechanical actuators in skin-integrated electronics for haptic interfaces. *Microsyst. Nanoeng.* **7**, 85 (2021).
28. Dhong, C. et al. Role of indentation depth and contact area on human perception of softness for haptic interfaces. *Sci. Adv.* **5**, eaaw8845 (2019).
29. Grigorii, R. V., Colgate, J. E. & Klatzky, R. The spatial profile of skin indentation shapes tactile perception across stimulus frequencies. *Sci. Rep.* **12**, 13185 (2022).
30. Lu, L., Leanza, S. & Zhao, R. R. Origami with rotational symmetry: a review on their mechanics and design. *Appl. Mech. Rev.* **75**, 050801 (2023).
31. Zhang, C. et al. Plug & play origami modules with all-purpose deformation modes. *Nat. Commun.* **14**, 4329 (2023).
32. Nolan, M. F. Quantitative measure of cutaneous sensation: two-point discrimination values for the face and trunk. *Phys. Ther.* **65**, 181–185 (1985).
33. Mancini, F. et al. Whole-body mapping of spatial acuity for pain and touch. *Ann. Neurol.* **75**, 917–924 (2014).
34. Wright, I. C. et al. The influence of foot positioning on ankle sprains. *J. Biomech.* **33**, 513–519 (2000).
35. Lysdal, F. G. et al. What have we learnt from quantitative case reports of acute lateral ankle sprains injuries and episodes of ‘giving-way’ of the ankle joint, and what shall we further investigate? *Sport. Biomed.* **21**, 359–379 (2022).

Publisher's note Springer Nature remains neutral with regard to jurisdictional claims in published maps and institutional affiliations.

Springer Nature or its licensor (e.g. a society or other partner) holds exclusive rights to this article under a publishing agreement with the author(s) or other rightsholder(s); author self-archiving of the accepted manuscript version of this article is solely governed by the terms of such publishing agreement and applicable law.

© The Author(s), under exclusive licence to Springer Nature Limited 2024

Methods

Transducer fabrication

The architecture of one transducer is illustrated in Extended Data Fig. 1. A soft (low-coercivity) ferromagnetic alloy (iron–cobalt 1:1; VACOFLUX 50, Vacuumsschmelze) was used for the inner core of the solenoid, the base of the armature and the cylindrical encasement. Each of these parts was machined by CNC lathe and wire electrical discharge machining (EDM). The magnetic components, together with a 3D-printed bobbin (Black Resin V4; Form 3B, Formlabs) and a flexible printed circuit board (fPCB) interconnect layer (PCBW), were assembled on the stage of the coil winder pictured in Extended Data Fig. 1a. The lead wires of the coil were then soldered to the fPCB interconnects, which wrapped from the bottom surface of the inner core to the opposing face of the bobbin. The armature was fabricated from an N48 nickel-plated neodymium magnet (Apex Magnets), a cylindrical ring of iron–cobalt and a 1.57-mm-diameter titanium pin. An elastomeric ring (Dragon Skin 10 SLOW, Smooth-On) was sandwiched between the base of the armature and the inner core.

The diaphragms were fabricated as caps that could be fitted across the top surface of each bobbin assembly. The elastomeric caps were cured inside a two-part mould. The top surface of the cap was a composite of PDMS and MNP. Iron oxide (II,III) MNP (50–100-nm particle size; Sigma-Aldrich) and part B of Sylgard 184 (Dow Corning) were mixed 15:100 by mass using a planetary mixer (2,000 rpm for 5 min under 0.2-kPa pressure; ARV-310P, THINKY) and were then allowed to return to room temperature. Part A of Sylgard 184 was then added in a 1:10 ratio by mass of part B and mixed using a planetary mixer (2,000 rpm for 30 s under 0.2-kPa pressure). The PDMS–MNP composite was reverse pipetted (12 µl) into the outer half of the mould and cured before filling the rest of the mould with unmodified PDMS (parts A and B, 1:10 by mass). The diaphragms were cured at 75 °C for 3 h.

Modular twist-locking harnesses, consumable adhesive layer and encapsulation

The harness consists of two parts that lock the vertical translation of the device on rotation (Extended Data Fig. 1). They were 3D-printed with Black Resin V4 (Form 3B, Formlabs). As shown in Extended Data Fig. 1d,e, harnesses were fabricated with spacers so that the effective indentation depth could be set to 1.0 mm, 1.5 mm or 2.0 mm.

The lower part of the harness adheres to the elastomeric substrate, which—in turn—adheres to the skin of the wearer. To reduce mechanical mismatch between the soft substrate and rigid harness, a hexagonal ring at the base of the harness was reinforced with a fibreglass mesh as a composite within the elastomeric substrate. As shown in Extended Data Fig. 2c, the adhesive layer started with a copper-clad fibreglass disc. On top of this substrate, we spin-coated (2,000 rpm for 2 min; WS-650-23 Spin Coater, Laurell) a thin (90-µm) layer of silicone-based elastomer (Dragon Skin 10 SLOW, Smooth-On). Before this layer was allowed to cure, fibreglass mesh (Fiberglass Warehouse) was layered into the thin layer of silicone. After curing this layer, the silicone–mesh composite was patterned by CO₂ laser (VLS3.50DT) into a hexagonal tiling. Then, another layer of silicone (Dragon Skin 10 SLOW, Smooth-On) was spin-coated onto the substrate at the full thickness of 140 µm (1,000 rpm for 2 min). After curing at 75 °C for 3 h, a 260-µm adhesive layer of silicone gel (Silbione RT Gel 4717, Elkem) was spun onto the substrate (1,000 rpm for 30 s). This was cured at room temperature for 24 h and then the pattern was removed by laser-cutting the outer shape. The elastomeric adhesive was then transferred onto a laminate backing and the harnesses were bonded to the non-adhesive surface by dip-coating it with single-component silicone (3140 RTV, Dow Corning).

The outer encapsulation (Fig. 1e) of the device comprises a silicone-based elastomer (Silbione RTV 4420, Elkem). The encapsulation was cured at 75 °C for 3 h between a two-part mould milled from aluminium. The resulting encapsulation layer had a thickness of 0.3 mm.

Phantom skin mechanical characterization and bistability measurements

The criteria for bistability and minimum transition currents were evaluated using skin phantoms with varying compressive moduli. Using the setup described in Extended Data Fig. 4c,d, the force–extension characteristics were determined and fitted to a theoretical indentation model, which accounts for the contact between a rigid cylinder with a flat end and an elastic half-space (35:1 PDMS mixing ratio, $E = 85$ kPa; 40:1, $E = 61$ kPa; 45:1, $E = 43$ kPa; 50:1, $E = 31$ kPa; 55:1, $E = 24$ kPa).

The experimental setup and results of the bistability experiments can be seen in Supplementary Fig. 1. Before testing, the transducer was attached to a phantom skin and transitioned between compressed and relaxed modes once to eliminate any unintended friction that may have arisen during installation. A 2-s pulse was then applied to the transducer to discount viscous effects and the minimum transition currents for both compressed and relaxed states were recorded. The study involved phantoms of thicknesses 2 mm and 5 mm with different moduli (PDMS mixing ratios of 35:1, 40:1, 45:1, 50:1 and 55:1) and three effective indentations (2.0 mm, 1.5 mm and 1.0 mm) adjusted with variations in the harness spacer (0 mm, 0.5 mm and 1.0 mm). Current-controlled stimuli were driven in the range –450 to 450 mA (2602 System SourceMeter, Keithley). To account for performance variation, three to four different transducers were used for each experimental condition.

Human participants

All participation was fully voluntary, with informed consent obtained before the experiments. Research protocols were approved by the Institutional Review Board at Northwestern University (STU00214800) and the Ethics Committee of Westlake University (20230731JHQ001).

Human skin mechanical characterization and bistability measurements

As shown in Extended Data Fig. 4e–g, the compressive moduli of human skin were assessed at three distinct locations (dorsal palm on adductor pollicis, dorsal palm on metacarpals and ventral forearm) in a cohort of six individuals (three male and three female, ages 20–36 years). The obtained experimental data were used to calculate the skin moduli using a theoretical indentation model, which accounts for the contact between a rigid cylinder with a flat end and an elastic half-space.

As shown in Fig. 2e, Extended Data Fig. 4a and Supplementary Fig. 2, the bistability and minimum transition current of the transducer were evaluated on five different locations of human skin: dorsal palm on adductor pollicis, dorsal palm on metacarpals, ventral forearm, dorsal aspect of upper arm and dorsal aspect of the neck near the C6 and C7 vertebrae. A total of six human participants (three male, three female, ages 20–36 years) participated in the study. Once attached to the skin, the transducer underwent a transition to the compressed and relaxed modes to eliminate any unintended friction between the armature and holder that may have occurred during installation. Following a 1-min break to allow for complete relaxation of the skin, the minimum currents required to induce the compressed and relaxed states of the transducer were measured using 500-ms pulses. Current-controlled stimuli were driven in the range –450 to 450 mA in increments of 50 mA (2602 System SourceMeter, Keithley). Two different harness heights (0 mm and 0.5 mm) were used during the testing process, providing effective indentations of 2.1 mm and 1.6 mm, respectively.

Using a similar protocol, the minimum input energy for transitions was evaluated for a subset of skin locations on the same six participants (dorsal palm on adductor pollicis, dorsal palm on metacarpals and ventral forearm). To determine the upper bound for a given skin location, the skin was preconditioned by indenting it for 30 s before each transition. To determine minimum input energy, the current magnitude was scanned between –450 and 450 mA in increments of 50 mA. For each current, the pulse duration was sequentially incremented by

Article

100 ms (starting with 50 ms) until the transducer transitioned or until the pulse duration reached 2,000 ms. The input work was calculated assuming ohmic losses and $R_{\text{coil}} = 13.39 \Omega$ (mean; 0.384Ω s.d.; $n = 18$). Supplementary Tables 1 and 2 report the current amplitude and pulse duration combinations that yielded the minimum input energy for each condition.

Evaluating perception of vibrotactile stimulus on human participants

The perception threshold for vibration was measured for $n = 12$ participants (6 male, 6 female, ages 20–36 years) using a transducer placed on the dorsal aspect of the palm of each participant, above the adductor pollicis. Both the relaxed and compressed states were tested for four different frequencies (50, 100, 150 or 200 Hz). Each participant was instructed to provide a ‘yes’ or ‘no’ judgement with no repeats (two-alternative forced choice). For each condition, an adaptive staircase was carried out in eight alternating ascending and descending sequences³⁶. While ascending, the staircase would reverse when the participant reported ‘yes’ and, while descending, the staircase would reverse when the participant reported ‘no’. Two interleaved staircases were carried out for each condition, one initially descending and the other initially ascending. Amplitude step sizes of 10 mA and 25 mA were used for the relaxed and compressed vibrations, respectively. Each stimulus was played for a 1-s interval. The participants were not given any visual or auditory cues from the transducer. Raw data for the experiments can be found plotted in Supplementary Figs. 3–5. For the synthesized results shown in Fig. 3e and Extended Data Fig. 7a,b, the thresholds of the last four sequences for each staircase were averaged.

Also, the perceived vibration of our device was evaluated by comparing it with a commercially available linear resonance actuator (LRA; VG0840001D, Vybrronics) using a methodology adapted from ref. 37. The results of this statistical analysis across $n = 12$ participants (6 male, 6 female, ages 20–36 years) are given in Supplementary Tables 5 and 6. See Supplementary Methods for further details.

Fabrication of the kirigami structure and its integration with the bistable transducer

The kirigami panels have a three-layer structure, as shown in Extended Data Fig. 6i,j. These layers consist of a central polyethylene terephthalate (PET) plastic sheet (0.2 mm thick), as well as upper and lower layers of polyurethane (PU) thin-film adhesive tape (0.1 mm thick). A commercial cutting machine (Silhouette Cameo 4) was used to cut the PET plastic sheet according to the designated pattern. Subsequently, PU thin-film adhesive tape was applied to the surfaces of the cut plastic units, obtaining the required flat kirigami panels for constructing the 3D kirigami structure, as illustrated in Extended Data Fig. 6k. Finally, oily glue was used to attach the taped panels to the hexagonal panels, completing the fabrication of the 3D kirigami structures, as shown in Extended Data Fig. 6l. For an overview of the design process, see Supplementary Methods.

For a Kresling module to transmit the linear motion of the bistable transducer into rotation of the hexagonal panels, rotation between the core and armature needs to be coupled. Extended Data Fig. 8f–k discusses how this can be achieved in a one-tiered structure using a physical limiter. Meanwhile, as depicted in Extended Data Fig. 6g, the two-tiered counter-rotating structure couples rotation of the core and armature without the need for such a limiter. In this design, the middle panel is created by attaching the bottom panel of the upper module to the top panel of the lower module. The flat surface of the solenoidal core is affixed to the middle panel and the upper surface of the armature is bonded to the top panel. In this structure, the permanent magnetic field of the armature was enhanced by adding a larger neodymium magnet (7 mm diameter, 1 mm thickness). Controlled by the transducer, this integrated device enables transition between the relaxed and compressed states. The contacting elements of the

integrated device (as shown in Extended Data Fig. 6h) can be attached to the skin surface using double-sided tape (3M 55236).

Evaluation of the perception of skin torsion on human participants

In the study, a total of 14 participants (8 male, 6 female, ages 23–31 years) were recruited. The experimental setup featured an adjustable device capable of simultaneous and independent adjustment of both height and two nested angles. This apparatus was complemented by an arm support, a wrist support and a laptop used for controlling the adjustable device. The ends of the double-layer stepper-motor shafts of the adjustable device were affixed with a ring and a disc, both of which matched in sizes and materials with the bottom ring and disc of the integrated transducer. Throughout the experimental procedure, the ring and disc were securely attached to the forearm of each participant using double-sided adhesive (3M 55236). The participants were not given any visual or auditory cues from the transducer.

We executed this study with a set of four ring–disc configurations (Supplementary Tables 7–10), each featuring three possible rotation angles. All participants were exposed to each configuration and set of rotation angles. The ranges for rotations and indentations were based on deformations evaluated from DIC results (Fig. 3l and Supplementary Video 4). Supplementary Table 7 reports outcomes for rotation and indentation of the ring (0.33° , 0.66° and 1° rotations; 0.2-mm indentation). Supplementary Table 8 reports outcomes for rotation of the disc (5° , 10° and 15° rotations; 0-mm indentation). Supplementary Table 9 reports outcomes for rotation and indentation of the disc (5° , 10° and 15° rotations; -0.4-mm indentation). Supplementary Table 10 reports outcomes for rotation and indentation of the ring and disc in angle combinations of $(0.33^\circ, 5^\circ)$, $(0.66^\circ, 10^\circ)$ and $(1^\circ, 15^\circ)$, with 0.2-mm and -0.4-mm indentation depths for the ring and disc, respectively. After experiencing each rotation angle within each ring–disc configuration five times, participants were asked to rate their perceived intensity on a seven-point scale, ranging from 1 to 7. Along with Supplementary Tables 7–10, the results are summarized in Fig. 3m, Extended Data Fig. 7d–g and Supplementary Fig. 6.

A non-parametric analysis method, the Friedman test, was used to assess differences among the rotation angles in each ring–disc configuration. The mean values across repeat measures for each participant were evaluated. The relevant test results are presented in Supplementary Table 11. Also, we conducted a post-hoc analysis among the same rotation angles using Dunn’s test. This analysis method allowed us to determine which specific pairwise comparisons among the rotation angles exhibited marked differences (Supplementary Table 11). To control the type I error rate, the P -values were adjusted using the Bonferroni method. To assess the difference in indentation at two distinct levels (0 mm and -0.4 mm) across three different rotation angles (5° , 10° and 15°), a paired t -test was conducted to compare the means from rotation angles of the disc with and without indentation. The statistical results are detailed in Supplementary Table 12. Finally, we adopted the Spearman rank correlation coefficient to evaluate monotonicity, with the results summarized in Supplementary Table 13.

Also, experiments comparing the perception of torsion at different locations ($n = 12$; 7 male, 5 female; ages 23–31 years) and experiments comparing the perceptions of skin torsion and indentation ($n = 15$; 7 male, 8 female; ages 23–31 years) were carried out. Raw data and results can be found in Supplementary Tables 14 and 15 and Extended Data Fig. 7. For further details, see Supplementary Methods.

Array and controller fabrication

The driving electronics for the haptic device were mounted and soldered to a fPCB (PCBWay). The operation of the board was controlled with a Bluetooth 5.0 controller (ISPI807, Insight SiP) integrated with the nRF52840 System-on-Chip (Nordic Semiconductor) and a built-in antenna. The device was powered by a rechargeable, 500-mAh

lithium-ion battery (LP802036JU, Jauch Quartz). The power management comprises a 5.1-V DC–DC boost converter (TPS61235, Texas Instruments) for driving the transducers and a low-dropout regulator (TPS7A023L, Texas Instruments) for logic-level power. A 500-mF supercapacitor was used to buffer the output of the 5.1-V boost converter (EDLC371420, TDK). An independent H-bridge (DRV8837, Texas Instruments) was used to drive each transducer with the 5.1-V power supply. The logic input for each H-bridge was delivered from GPIO expanders (TCA9555, Texas Instruments), which—in turn—communicated with the controller with a serial two-wire interface line. Inductance measurements were performed using a dedicated integrated circuit (LDC1101, Texas Instruments), which communicated with the controller with a serial peripheral interface line. Analogue demultiplexers (MAX4691EGE+, Analog Devices) were used to demultiplex the input from each transducer into the inductance measurement unit.

Each transducer was configured as a modular unit that could be incorporated into a hexagonal tiling of self-similar units. Each element was independently addressed from exposed contacts on the exterior tiles of the 19-element hexagonal grid. To route the driving signals to interior elements of the array, the embedded interconnects of each element were configured so that traversing signals would reach the correct elements by soldering each identical element at prescribed rotations of 120°. The orientation diagram is illustrated in Extended Data Fig. 2d. The serpentine interconnects are two-layer fPCBs manufactured from 35-μm copper traces with a total thickness of 130 μm (PCBWay).

Visual sensory substitution system and task

For the visual sensory substitution system, as shown in Fig. 4f, Extended Data Fig. 9a and Supplementary Video 6, the user has the haptic device mounted on the back of their neck and they hold the smartphone (iPhone 12 Pro, Apple) in their hand. LiDAR and IMU sensors anchor six virtual detection windows to the room, which remain fixed in space at a distance defined by the user (2.5 m for this task), even when the phone moves (top left, top middle, top right, bottom left, bottom middle and bottom right). When an object crosses the boundary of the window, it sends a cue to the haptic device corresponding to the location of that window. The haptic cues render as a wave of indentation that travels between the bottom and top in the left, middle or right columns of the haptic array. To indicate the bottom row, the wave starts at the top and ends at the bottom. To indicate the top row, the wave starts at the bottom and ends at the top (Supplementary Video 6).

We evaluated this task on healthy individuals with blindfolds ($n = 7$, 4 male, 3 female, ages 19–37 years). In the experiment, each window was triggered manually by the investigator presenting a ball through the respective location. The task was carried out in three phases, with the first two being part of the training. The first part of the training, which lasted 5–10 min, included an introduction to the system and a short period of exploration, during which time the participant could direct cues. In the second phase of training, the participants were asked to indicate the location of perceived cues while closing their eyes (10–20 min). Four repeats of each cue were presented randomly. During this phase, the participants were given verbal feedback about the accuracy of their answers. In the last phase, in which we recorded answers as part of our experiment, we asked the participants to close their eyes and wear a blindfold. Along with the participants being blindfolded, they were given earplugs (SA-7-5, Lysian) and noise-cancelling headphones (WH-CH720N, Sony). The headphones continuously played pink noise during the experiments. The participants were given cues randomly in each of the six locations. Each of the locations was repeated six times in random order. The significance of the accuracy of each participant ($n = 7$) was evaluated using the Wilcoxon signed-rank test, given the null hypothesis that selections were made at random between six choices (that is, accuracy arose from a distribution with median 16.7%). Also, the effect size was characterized according to rank-biserial correlation, calculated from the z-statistic of the signed-rank test.

Balance sensory substitution system and task

For the balance sensory substitution system, as illustrated in Fig. 4g, a smartphone (iPhone 12 Pro, Apple) held against the body of the participant tracks its orientation using an IMU. These data serve feedback to the haptic device, which—analogous to a spirit level—renders a line of vibration that follows the postural angle of the user (see Extended Data Fig. 9i for feedback patterns).

We evaluated this task on healthy individuals ($n = 10$, 5 male, 5 female, ages 20–36 years). We used the sharpened Romberg test (eyes closed) to measure standing stability and postural control. As shown in Fig. 4g, the participants were asked to remove their shoes and stand with two feet in a line (toe to heel). Their arms were crossed in front of the body and their eyes were closed. Each patient would try to maintain their balance and they were evaluated on the time they could stand without opening their eyes, shifting their feet or moving their arms. After instruction on the task and devices, the participants would be allowed one trial with and without feedback. During the experiment, 20 repeated trials were recorded for each participant. To reduce fatigue, the participants were asked to sit and rest for 2 min between every four attempts. The sequence of attempts with feedback and without feedback were counterbalanced between rest intervals (Supplementary Table 16). Statistical significance for the outcomes of these experiments was evaluated by modelling the presence and absence of feedback as a factor in a repeated-measures ANOVA model (nine degrees of freedom). The balance duration, acting as the dependent variable, was transformed logarithmically to account for its right-skewed distribution. Ultimately, the P value was determined under the null hypothesis that no differences exist in group means (Extended Data Fig. 9).

Foot-strike sensory substitution system and task

For the foot-strike sensory substitution system, as illustrated in Fig. 4h, the user wears an external IMU (AirPods, Apple) in their right shoe and holds a smartphone (iPhone 12 Pro, Apple) in their hand. The smartphone uses LiDAR to track the orientation of an adjacent surface and the external IMU to track foot orientation. The haptic device receives these streams of information and renders vibration in the direction of error between the foot and the surface (Extended Data Fig. 10a).

The foot-strike task aimed to testing whether the system could be used to help a participant match their foot-strike orientation without receiving any other external feedback. We tested the system on healthy individuals with their eyes closed ($n = 3$, 2 male, 1 female, ages 21–37 years). As shown in Fig. 4h and Extended Data Fig. 10a, a variable surface would be presented in front of the participant at fixed orientations of $(\psi, \phi) \in \{(0^\circ, 0^\circ), (15^\circ, 60^\circ), (15^\circ, -60^\circ), (30^\circ, 0^\circ)\}$, in which ψ is the pitch of the surface and ϕ is the yaw (Extended Data Fig. 10a for the reference frame for pitch and yaw). During the experiment, the LiDAR modality on the smartphone was used to evaluate the orientation of the surface and send feedback to the haptic device. Feedback in the form of vibration would be provided to the haptic device and the location of vibration would indicate where error exists between the orientations of the surface and foot (Extended Data Fig. 10b). On contact with the surface, the haptic device would deliver indentation in the pattern detected. The participants were trained on the system for 25–40 min and then they were asked to match their foot to the presented surface by stepping forward onto the surface. Error was measured as the angle between the foot and the surface. The task was carried out in five phases, with the first two being part of the training. The first part of the training, which lasted 5–10 min, included an introduction to the system and a short period of exploration, during which time the participant could direct cues. In the second phase of training, the participants were asked to match the location of perceived cues while closing their eyes (20–30 min). Repeats of each cue were presented randomly. During this phase, the participants were given feedback about the accuracy

Article

of their answers. In the last three phases, we recorded the error for each cue as part of 60 trials (20 trials per phase). In each experimental phase, the participant was presented with each of the fixed orientations randomly until they completed five trials for each surface. During each phase, the participant was asked to attempt to complete the motion within designated time intervals, 1.5 s, 1.0 s and <1.0 s progressively.

Control experiments without the haptic device were performed in subsequent sessions for each participant. The structure of these sessions, including training parameters, mirrored the feedback group. Control conditions were tested for 20 repeat trials, including five presentations of each surface orientation (Supplementary Table 18).

The actual step intervals are reported for each participant in Supplementary Table 17. The significance of these results was evaluated for each participant using the Wilcoxon signed-rank test, given the null hypothesis that the median of the population of differences with and without feedback are zero, $n = 3$. The effect size was characterized according to rank-biserial correlation, calculated from the z-statistic of the signed-rank test. See Extended Data Fig. 10c–e for individual statistical results.

Reporting summary

Further information on research design is available in the Nature Portfolio Reporting Summary linked to this article.

Data availability

All data generated or analysed during this study are included in this published article (and its supplementary information files).

36. Leek, M. R. Adaptive procedures in psychophysical research. *Percept. Psychophys.* **63**, 1279–1292 (2001).
37. Kim, J. T. et al. Mechanics of vibrotactile sensors for applications in skin-interfaced haptic systems. *Extreme Mech. Lett.* **58**, 101940 (2023).
38. Jang, K. I. et al. Soft network composite materials with deterministic and bio-inspired designs. *Nat. Commun.* **6**, 6566 (2015).

39. Girard, G., Martiny, M. & Mercier, S. Experimental characterization of rolled annealed copper film used in flexible printed circuit boards: identification of the elastic-plastic and low-cycle fatigue behaviors. *Microelectron. Reliab.* **115**, 113976 (2020).

Acknowledgements M.F. acknowledges support from the National Institutes of Health (grant T32HL007909). H.J. acknowledges support from the National Natural Science Foundations of China (grant 12350003). H.J. and Z.G. thank the Research Center for Industries of the Future (RCIF) at Westlake University and Westlake Education Foundation for supporting this work. Z.X. acknowledges the support from the National Natural Science Foundation of China (grants 12472160 and 12072057), Liaoning Revitalization Talents Program (grant XLYC2007196) and Dalian Outstanding Young Talents in Science and Technology (grant 2021RJ06). We also thank R. Golemia and T. Bui from the machine shop at Northwestern University for CNC lathe and wire electrical discharge machining fabrication.

Author contributions M.T.F.: conceptualization, methodology, software, validation, formal analysis, investigation, visualization, resources, data curation, writing—review and editing, writing—original draft. K.-H.H.: methodology, investigation, formal analysis, visualization, writing—review and editing. Z.G.: methodology, investigation, formal analysis, visualization, writing—review and editing. S.L.: methodology, investigation, formal analysis, visualization, writing—review and editing. J.-T.K.: methodology, investigation, formal analysis, visualization, writing—review and editing. T.S.: investigation, formal analysis, visualization. D.S.: methodology, validation, visualization, data curation, writing—review and editing. F.A.-N.: investigation, Y.M.: investigation, visualization. S.B.: investigation. C.F.: investigation. D.B.: investigation. Z.Z.: investigation. Y.Z.: investigation, visualization. E.F.: formal analysis, writing—review and editing. K.E.M.: investigation, writing—review and editing. Y.H.: investigation. L.E.: investigation. J.Z.: investigation. J.-Y.Y.: methodology. M.P.: methodology. J.S.: writing—review and editing. A.G.H.: writing—review and editing. H.-S.S.: methodology. J.E.C.: methodology, formal analysis, writing—review and editing. Y.H.: funding acquisition, project administration, supervision, writing—review and editing. Z.X.: funding acquisition, project administration, supervision, writing—review and editing. H.J.: funding acquisition, project administration, supervision, writing—review and editing. J.A.R.: funding acquisition, project administration, supervision, writing—review and editing.

Competing interests The authors declare no competing interests.

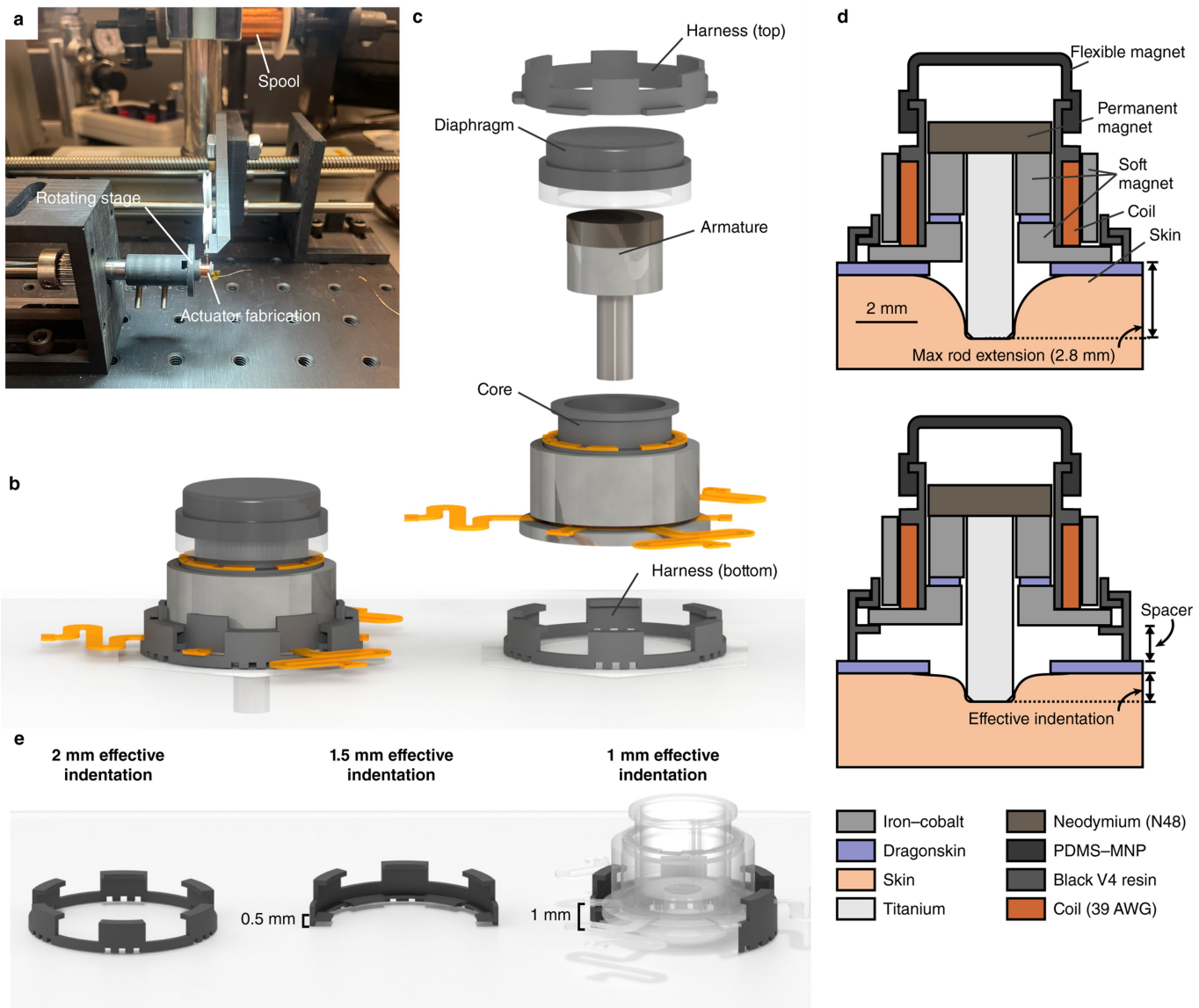
Additional information

Supplementary information The online version contains supplementary material available at <https://doi.org/10.1038/s41586-024-08155-9>.

Correspondence and requests for materials should be addressed to Yonggang Huang, Zhaoqian Xie, Hanqing Jiang or John A. Rogers.

Peer review information *Nature* thanks Kuanming Yao and the other, anonymous, reviewer(s) for their contribution to the peer review of this work.

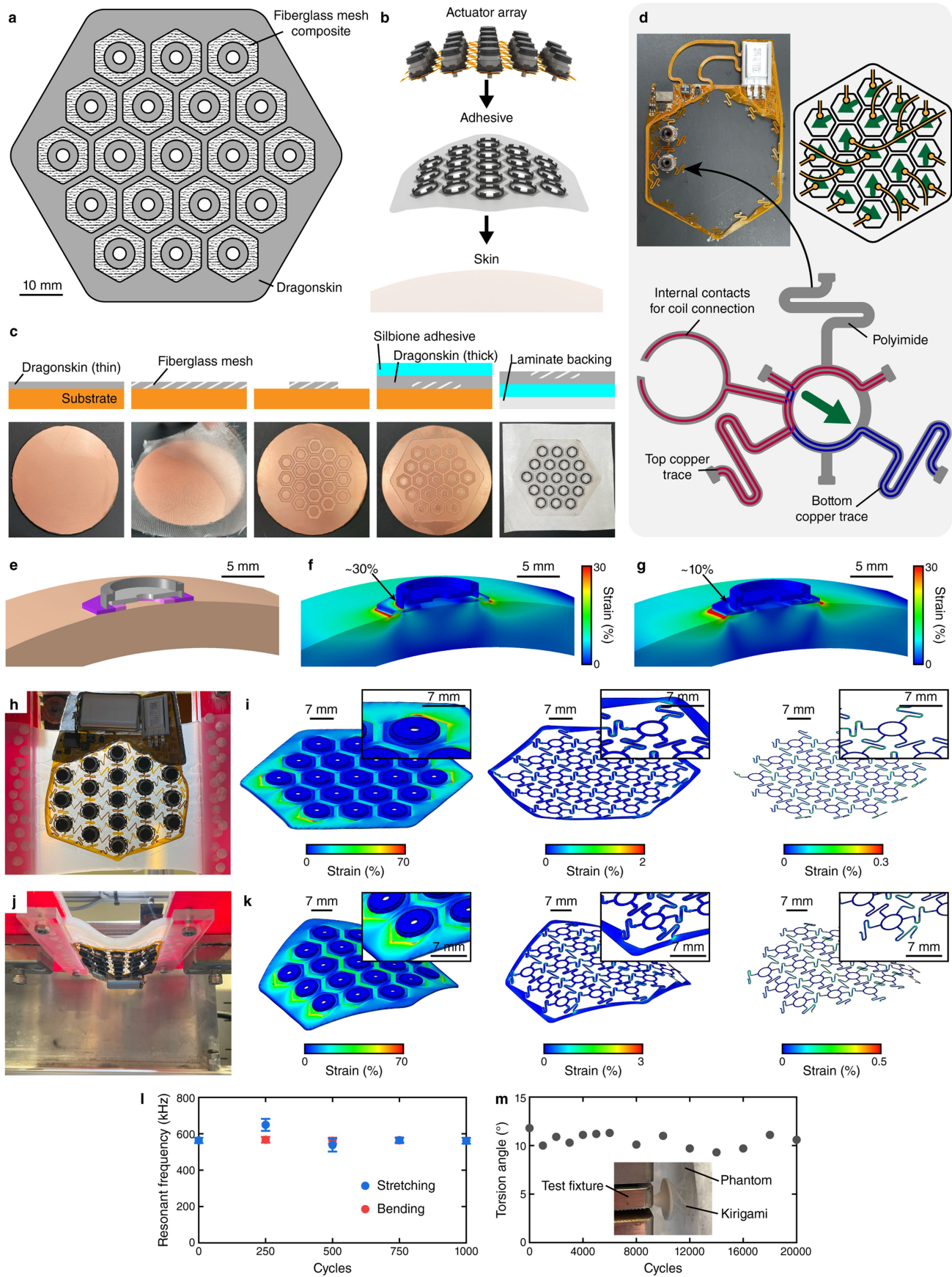
Reprints and permissions information is available at <http://www.nature.com/reprints>.



Extended Data Fig. 1 | Transducer design and fabrication. **a**, Fabrication of the core on a motorized stage. Each coil was wound to eight layers along the 2.75-mm shaft of the bobbin to reach approximately 63% fill density. The resistance of each coil was measured to verify consistency and all transducers described in this article lie within 13–14 Ω ($R_{\text{coil}} = 13.39 \pm 0.384 \Omega$; $n = 18$).

b, Assembled transducer. **c**, Disassembled view of the transducer with key mechanical components labelled. **d**, Scale illustration of bistable transducer components and the variable harness system. **e**, 3D illustration of the three harness variants used in this study.

Article

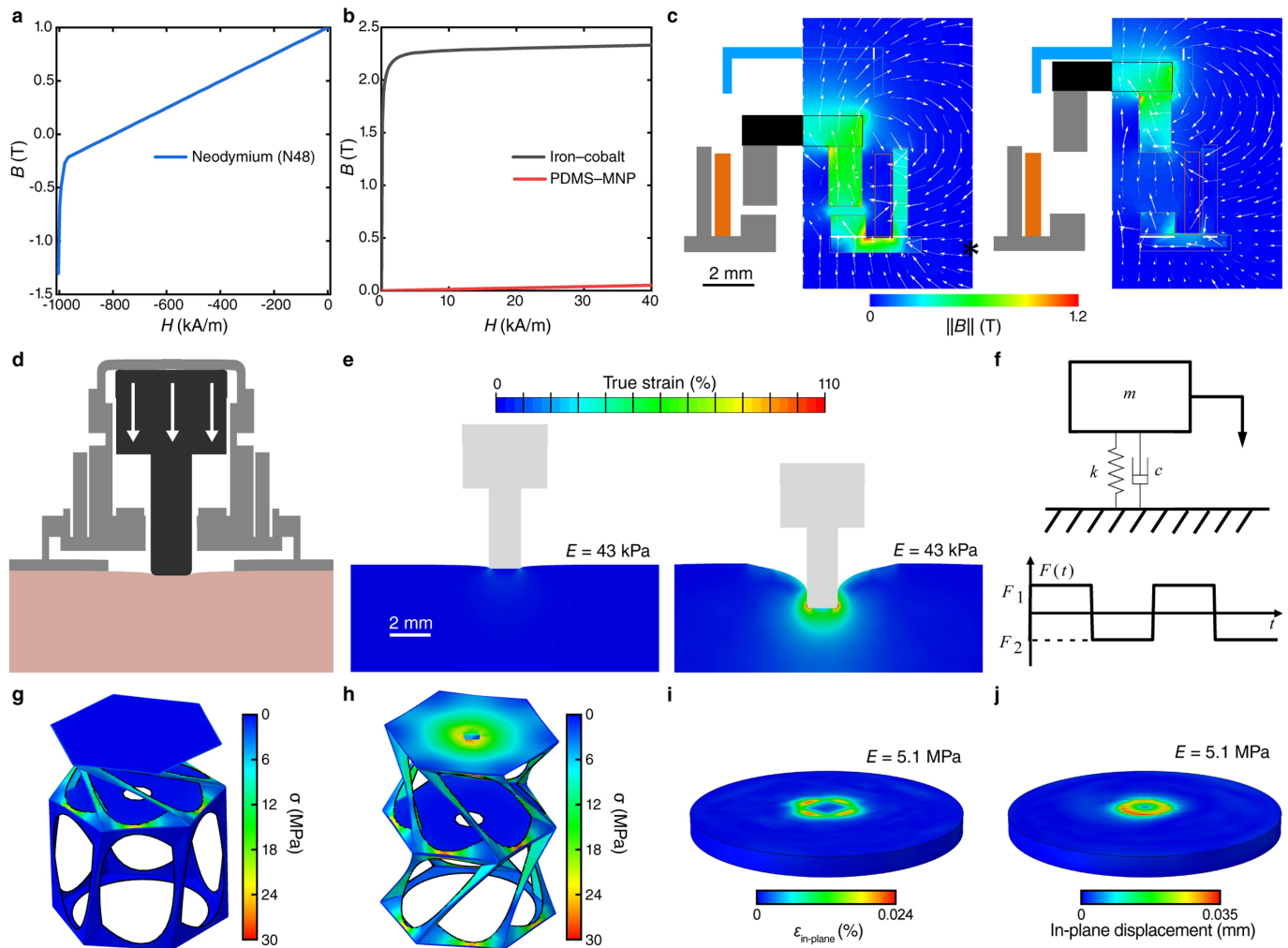


Extended Data Fig. 2 | See next page for caption.

Extended Data Fig. 2 | Transducer array design and mechanical testing.

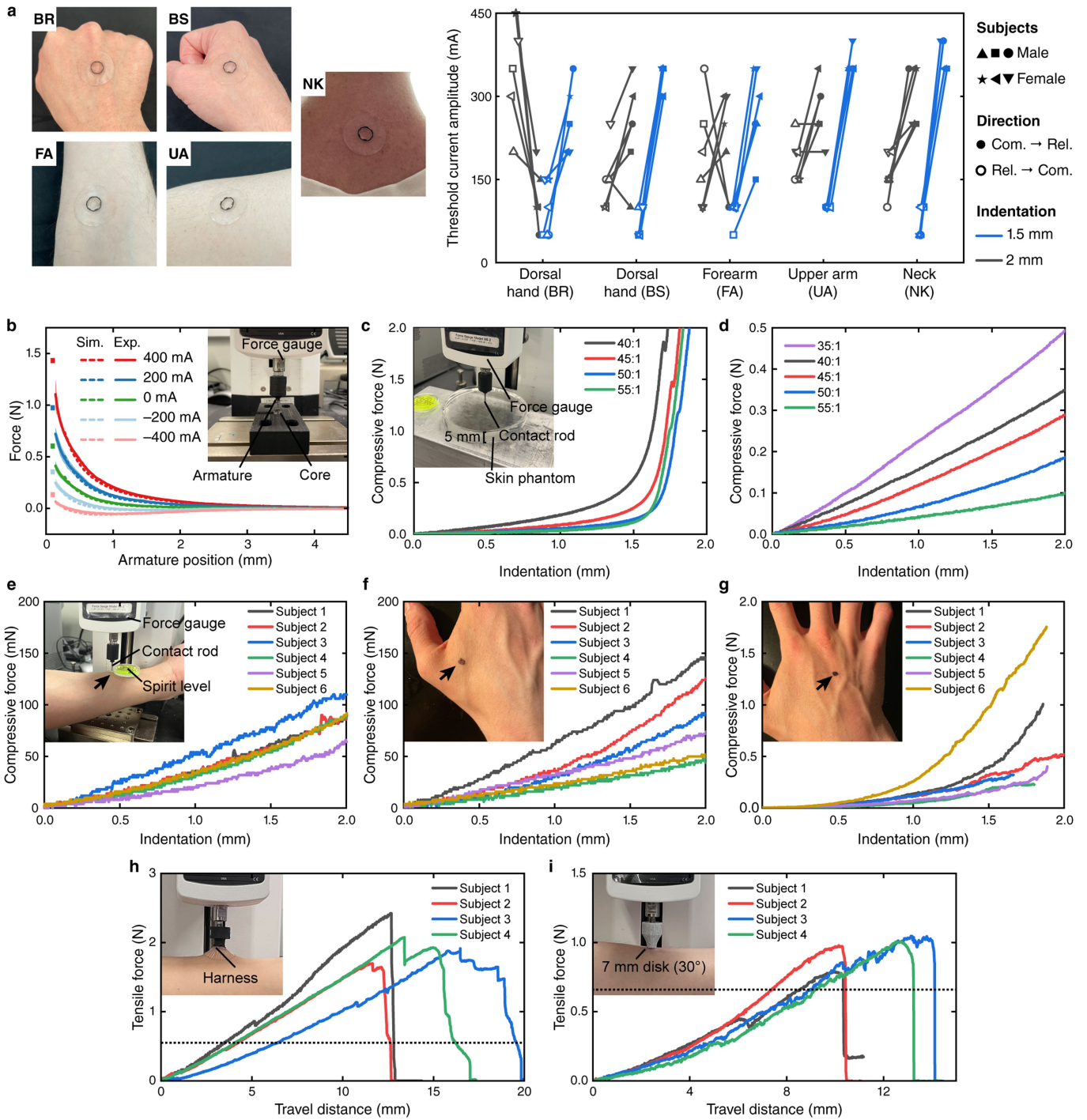
a, Schematic illustration of the mesh-reinforced regions of the adhesive layer. **b**, Integration of the array with skin using the adhesive layer. **c**, Layer-by-layer fabrication of the adhesive coupling, schematic illustrations and photographs. **d**, Photograph of two transducer units positioned inside the controller module and schematic illustrations demonstrating how each modular interconnect layer routes signals through the hexagonal array. During assembly, the internal contacts fold into the core, in which they can be soldered to the coil. **e–k**, Mechanical response testing for the array. **e**, Model geometry for mechanical simulation of strain under a unit actuator during skin bending (50 mm radius). **f**, Simulated strain using a substrate without mesh. **g**, Simulated strain with a mesh-reinforced substrate. **h**, Photograph of the haptic array under 20% lateral stretching. **i**, Numerical simulation of strain

within the Dragon Skin/mesh adhesive layer, polyimide interconnects (fracture strain, >7%; ref. 38) and copper traces (fracture strain, >1%; ref. 39) of the array during 20% lateral stretching. **j**, Photograph of the haptic array under 50-mm bending radius. **k**, Numerical simulation of strain within the Dragon Skin/mesh adhesive layer, polyimide interconnects and copper traces of the array during bending (50 mm radius). **l**, Transducer resonance measured across the array periodically by the embedded inductance measurement unit during cyclic deformations of stretching and bending (mean across 19 transducers; bars, standard deviation). **m**, Torsion angle induced by a kirigami structure (8.5 mm initial height) on a skin phantom ($E = 31 \text{ kPa}$) measured periodically during cyclical translation of the top panel by 3 mm (setup shown in inset).



Extended Data Fig. 3 | Finite element modelling of electromagnetic and solid mechanical processes. **a**, Demagnetization curve of an N48 neodymium magnet. Arnold Magnetic Technologies N48 from the ANSYS material library was used for the permanent magnet part of the armature with a modification of B_r to 1 T in its B - H curve. **b**, B - H curve of iron–cobalt (VACOFLUX 50 Solid) and PDMS–MNP. The PDMS–MNP diaphragm used a self-defined material with a relative permeability of 1.04 and a bulk conductivity of 4 S m^{-1} . **c**, Example quasi-magnetostatic simulation showing the magnetic field strength and direction as a colour map and quiver plot ($I_{\text{coil}} = 400 \text{ mA}$) for the compressed and relaxed states (* $\|B\| = 7.4 \text{ mT}$, stray magnetic field at 6.6 mm radial distance from central axis). **d**, Model geometry and boundary conditions for solid

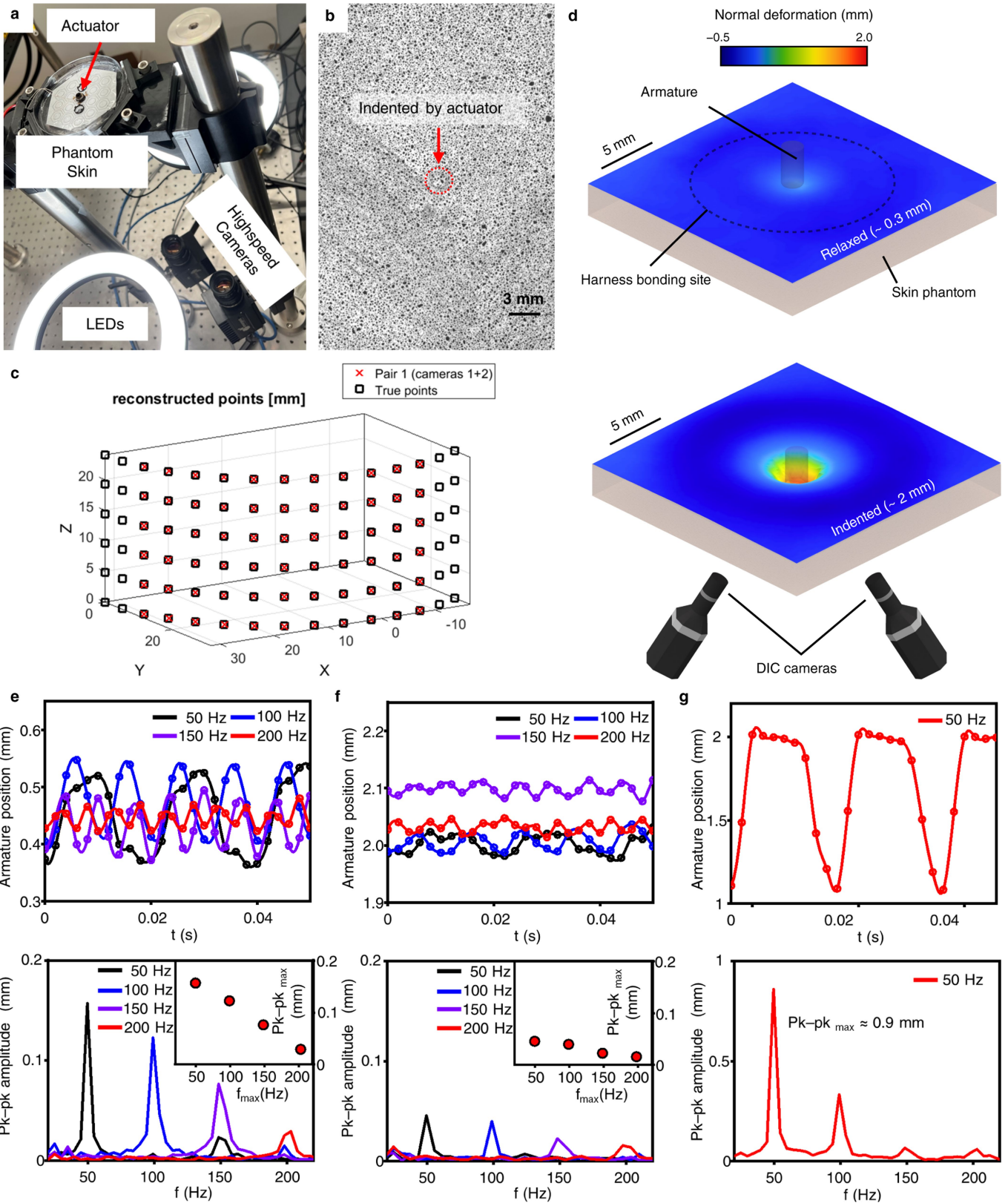
mechanical processes. A downward displacement was applied to the armature and the corresponding reaction forces from the skin phantoms were evaluated. **e**, Example simulations showing strain distribution within a skin phantom (45:1, $E = 43 \text{ kPa}$) for the relaxed and compressed states (2 mm effective indentation). **f**, Schematic of the mass–spring–damper vibration model for the transducer and the periodic loading force applied to it. **g**, Stress distribution within the kirigami structure in the relaxed state (PET yield stress, 80 MPa). **h**, Stress distribution within the kirigami structure in the compressed state. **i**, In-plane strain of the skin phantom in the compressed state. A stiff skin phantom was used here to evaluate the upper bound of stress in the structure ($E = 5.1 \text{ MPa}$). **j**, In-plane deformation of the skin phantom in the compressed state.



Extended Data Fig. 4 | See next page for caption.

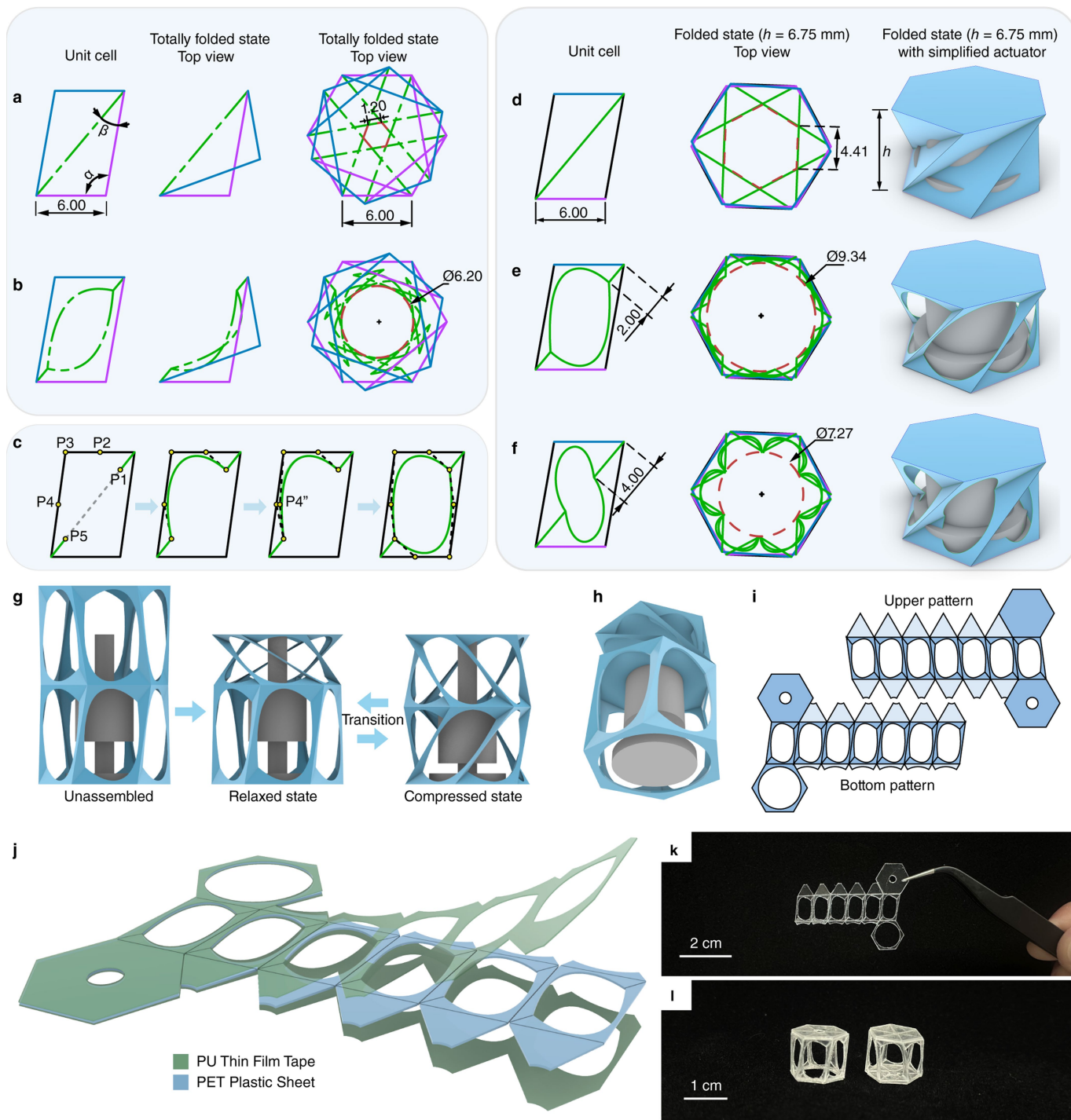
Article

Extended Data Fig. 4 | Mechanical characterization of transducers, skin phantoms and human skin. **a**, Mechanical bistability evaluation in healthy individuals. Measurements were performed in five skin locations (depicted on the left). The absolute value of current required to transition the armature between relaxed and compressed states was measured for $n = 6$ participants (three males, three females, ages 20–36 years). The indentation depth was adjusted by performing experiments with harnesses of varying heights. **b–i**, Characterization of force as a function of extension was performed using a motorized stage (ESM303, Mark-10) and a force gauge (M5-2, Mark-10) with a 10 N capacity. **b**, Experimental and simulated forces measured as a function of the longitudinal position of the armature for several applied current values (excluding PDMS–MNP diaphragm and skin compressive force). We defined the origin as where the base of the armature and the core are in contact and we determined this using the force meter. For experimental results, the solid lines and shaded areas correspond to the means and standard deviations, respectively ($n = 8$). The square markers correspond to the maximum recorded force for each current, averaged across all transducers. The inset shows the experimental setup. **c**, Forces measured as a function of the longitudinal position of the armature rod (excluding force from core) for 40:1, 45:1, 50:1 and 55:1 skin phantoms with thicknesses of $d = 2$ mm (inset shows experimental setup). **d**, Forces measured as a function of the longitudinal position of the armature rod for 35:1, 40:1, 45:1, 50:1 and 55:1 skin phantoms with thicknesses of $d = 5$ mm. **e**, Skin reactive forces measured as a function of the longitudinal position of the armature rod (excluding force from core) for the ventral aspect of the forearm for $n = 6$ subjects (three males, three females, ages 20–36 years; experimental setup shown in inset). **f**, Skin reactive forces measured for the dorsal aspect of the palm above the adductor pollicis for $n = 6$ subjects (three males, three females, ages 20–36 years; location indicated in inset). **g**, Skin reactive forces measured for the dorsal aspect of the palm above metacarpal III for $n = 6$ subjects (three males, three females, ages 20–36 years; location indicated in inset). **h**, Tensile-peeling-force measurements of the harness attached to the silicone–mesh composite adhesive mounted on the forearm of $n = 4$ subjects (two males, two females, ages 26–32 years). The horizontal line shows the holding force of the indentation actuator. **i**, Tensile peeling force for a Ø7 mm disc pre-rotated to 30° and mounted on the forearm of $n = 4$ subjects (two males, two females, ages 26–32 years) with 3M 9699 double-sided adhesive. The horizontal line shows the holding force of the torsion actuator.



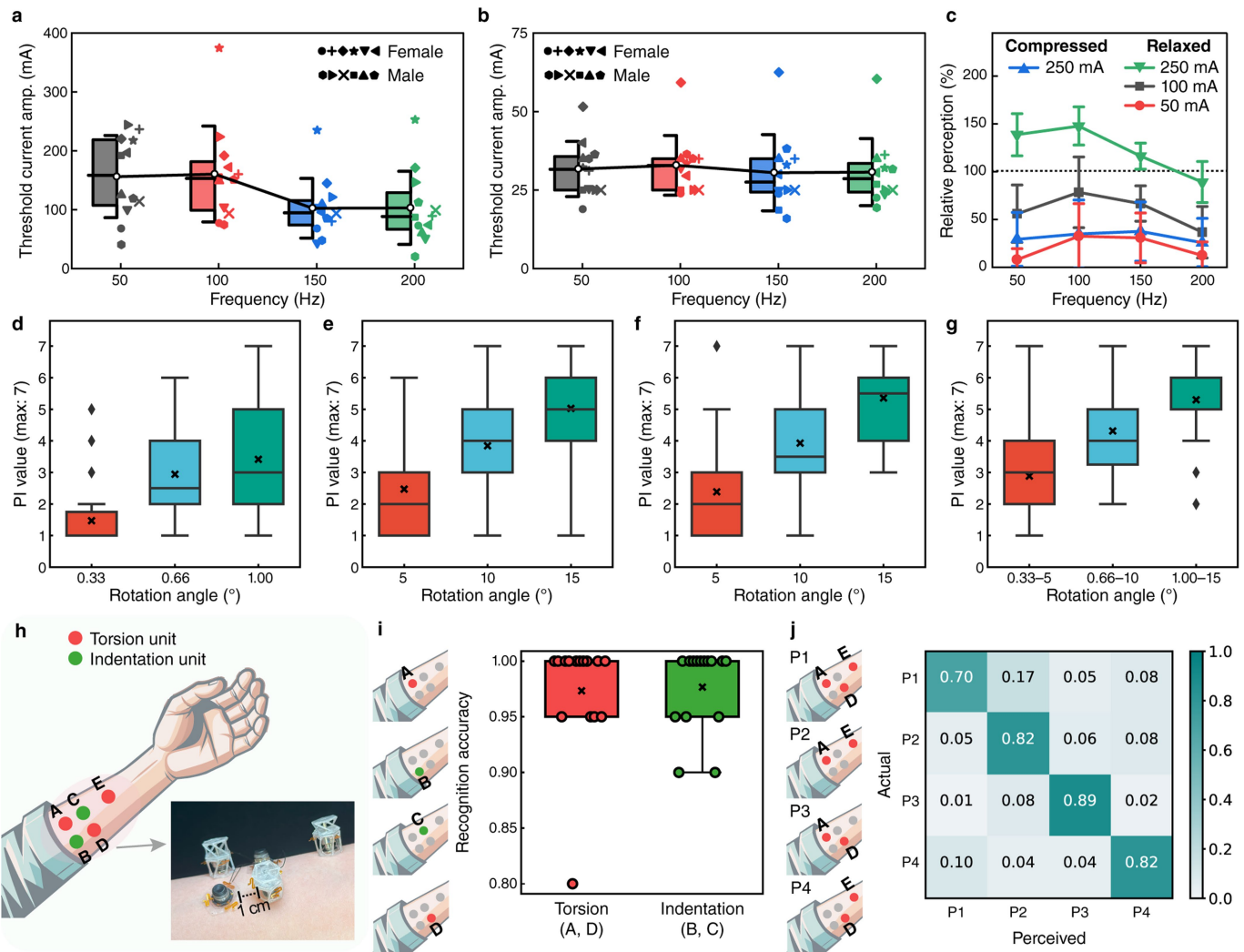
transformations (bottom) of skin phantom indentation (45:1 PDMS phantom, $E = 43 \text{ kPa}$; $I_{\text{coil-pk}} = 250 \text{ mA}$) measured at the centre of the contacting rod of the transducer with DIC during square-wave perturbation of the coil. **e**, Relaxed-state perturbation. **f**, Compressed-state perturbation. **g**, Full-transition vibration.

Article



Extended Data Fig. 6 | Design and fabrication of the kirigami transmission structure. **a**, Basic split-crease unit cell design and fully folded Kresling-pattern-inspired kirigami structure. Parameters α and β are discussed in the Supplementary Methods. **b**, Design of a variant cell that uses a combination of straight and curved creases, which further increases the internal space. **c**, Curved crease design using the Bézier curve method, in which P1–P5 are control points (discussed in the Supplementary Methods). **d**, Kirigami structure with only straight valley creases in the folded state ($h = 6.75$ mm).

e, Variant kirigami structure with 2 mm straight crease length ($h = 6.75$ mm; folded state). **f**, Crease length, 4 mm. **g**, Two-tiered kirigami structure illustrating switchable motion states. **h**, Bottom view of the contacting elements (ring and disc). **i**, 2D patterns of the lower and upper tier kirigami modules for fabrication. **j**, Panels used to make the kirigami structure, consisting of one layer of PET plastic sheet and two layers of PU thin-film tape. **k**, Photograph of the flat kirigami panel used for fabricating the 3D structure. **l**, Photograph of the assembled lower and upper tier kirigami modules.



Extended Data Fig. 7 | Perceptual intensity of vibration and torsion.

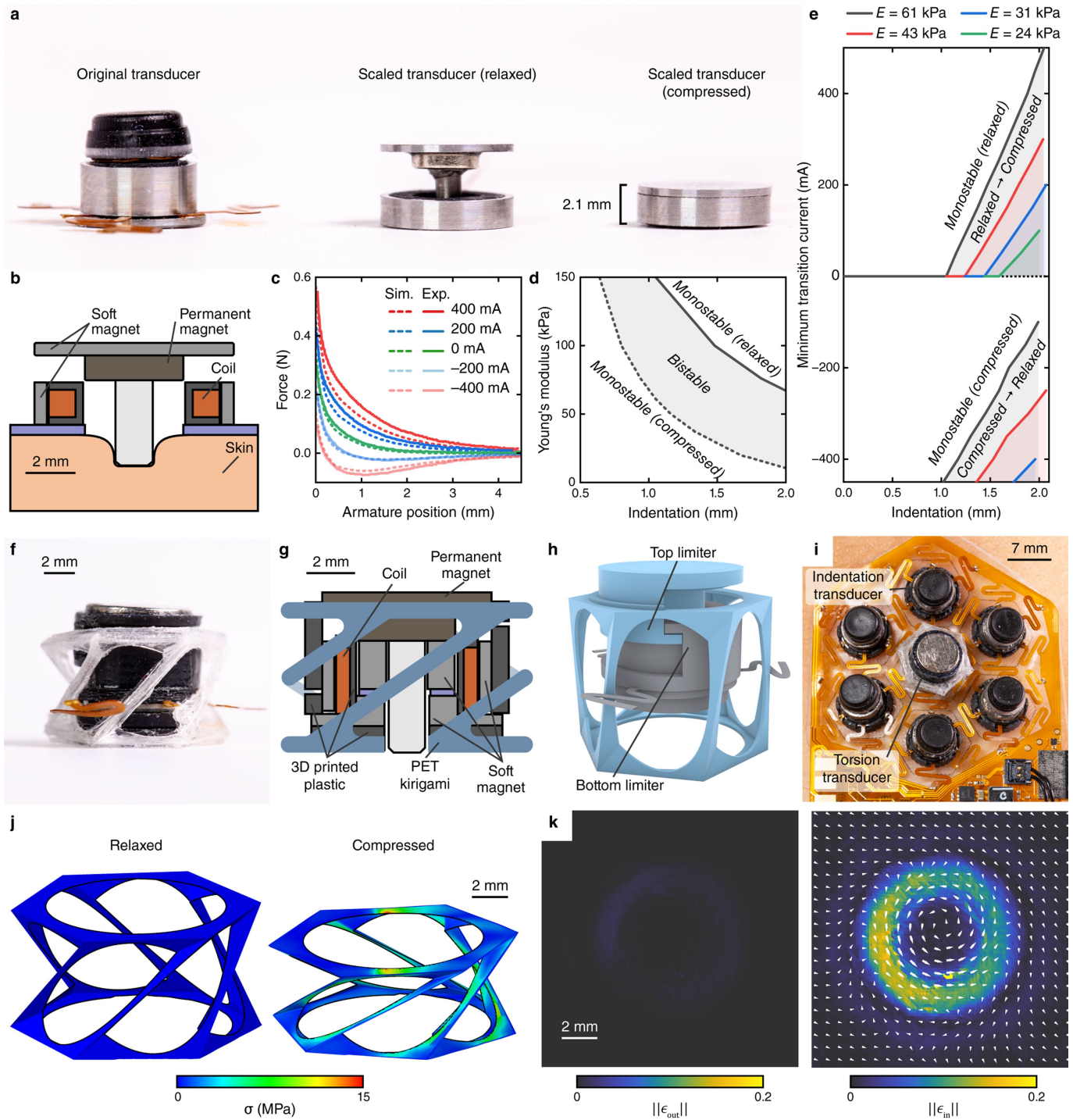
a, b, Vibration current amplitudes of perception thresholds ($n=12$, six males, six females, ages 20–36 years). **a**, Compressed-state vibration. **b**, Relaxed-state vibration. **c**, Relative perception of vibration in the transducer with respect to a commercial LRA (dotted line, equivalent perception; $n=12$, six males, six females, ages 20–36 years). **d–g**, Perceptual intensity evaluated according to its definition in Methods for $n=14$ human participants (eight males, six females, ages 23–31 years) under four ring–disc configurations. The left column shows mean values reported by each subject ($n=5$ repeat measurements; bars, standard deviation) and the right column reflects all subjects ($n=14$; bars, 1.5 interquartile range; shaded box, range between 25th and 75th percentiles; horizontal line, median; \times , mean; \blacklozenge , outliers from 1.5 interquartile range). According to the Friedman test, a statistically significant difference can be seen within each ring–disc configuration ($P<0.0001$) and each showed a moderate positive correlation between ratings and rotation angles (Spearman correlation, $\rho\ge0.58$), which was highly statistically significant ($P<0.0001$).

d, Outcomes reported for rotation and indentation of the ring, in which the ring was rotated to angles of 0.33° , 0.66° and 1° with a static indentation of 0.2 mm .

e, Outcomes reported for rotation of the disc, in which the disc was rotated to angles of 5° , 10° and 15° with a static indentation of 0 mm . **f**, Outcomes reported for rotation and indentation of the disc, in which the disc was rotated to angles of 5° , 10° and 15° with a static indentation of -0.4 mm . **g**, Outcomes reported for rotation and indentation of the ring and disc, in which the ring and disc were rotated to angles of $(0.33^\circ, 5^\circ)$, $(0.66^\circ, 10^\circ)$ and $(1^\circ, 15^\circ)$ with a static indentation of $(0.2\text{ mm}, -0.4\text{ mm})$.

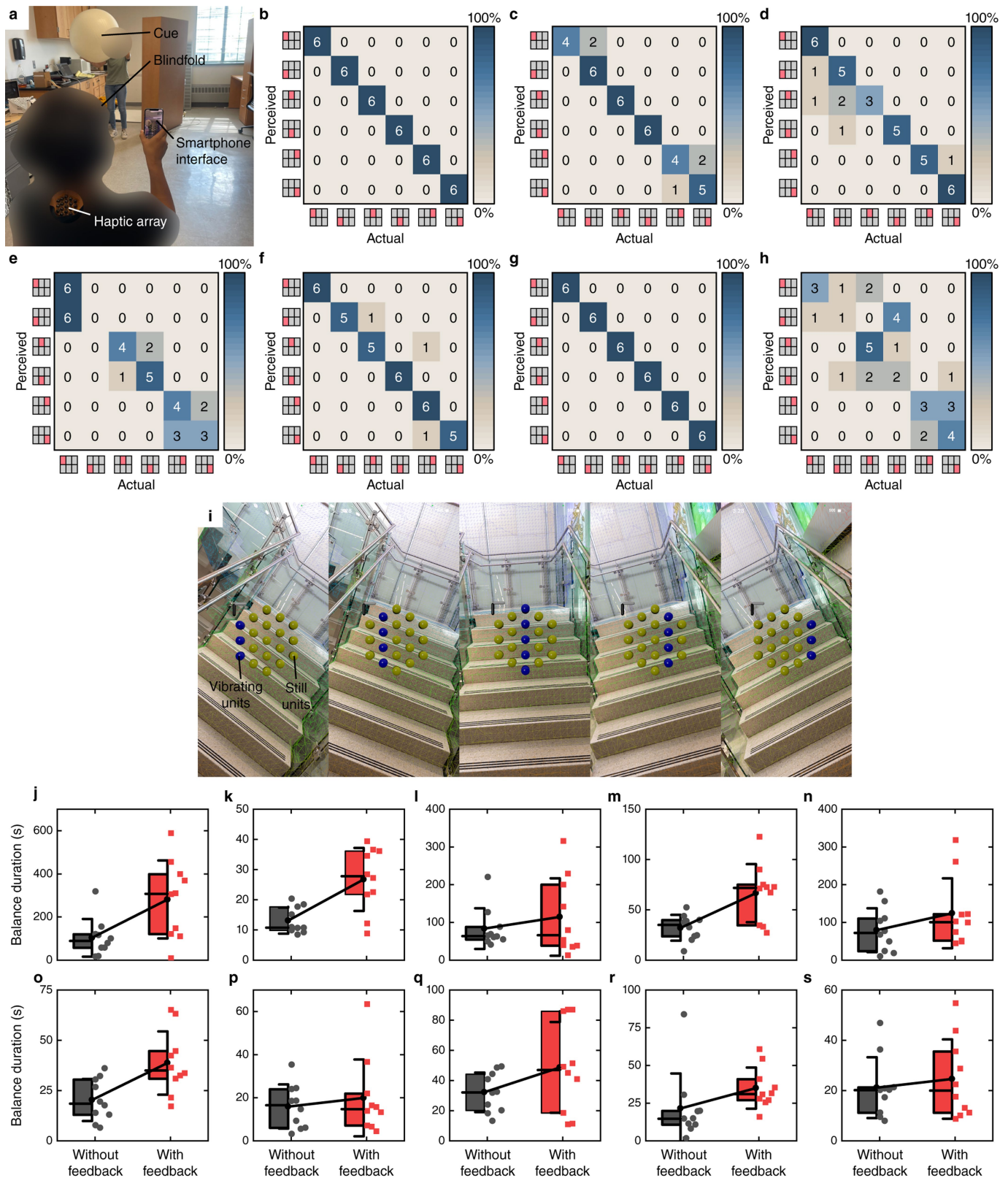
h–j, Torsion and indentation array discrimination experiments. **h**, Illustration and photograph of the apparatus setup, which includes three torsion actuators (A, D and E) and two indentation actuators (B and C). **i**, Discrimination between indentation and torsion, combined results for 15 healthy participants (seven males, eight females, ages 23–31 years). Accuracy was averaged over 15 subjects with ten repeated trials ($n=150$). **j**, Discrimination between patterns of torsion, combined results for 12 healthy participants (seven males, five females, ages 23–31 years).

Article



Extended Data Fig. 8 | Miniaturization of indentation and torsional transducers. **a–e**, Miniaturization of the indentation structure. The coil was wound to 12Ω . **a**, Photograph of the original and miniaturized transducers. **b**, Scale illustration of the miniaturized transducer. **c**, Experimental and simulated forces measured as a function of the longitudinal position of the armature for several applied current values. Measurements were performed using a motorized stage (ESM303, Mark-10) and a force gauge (M5-2, Mark-10) with a 10 N capacity. **d**, Simulated phase diagram for $I_{coil} \rightarrow \infty$ showing regions across the parameter space of skin modulus and indentation depth for successful bistability. The shaded regions correspond to the boundaries of bistability, outside which only one state is attainable (monostable, compressed or relaxed). **e**, The minimum applied current required to overcome the energy

barrier between each state plotted against the total indentation depth for a range of Young's moduli, E (simulated). **f–k**, Miniaturization of the torsion structure. **f**, Photograph of the single-tiered kirigami structure. **g**, Scale illustration of the one-tiered kirigami structure. **h**, Volumetric illustration of freely moving mechanical elements of the one-tiered structure. **i**, Photograph of a haptic array incorporating units for both indentation and torsion. **j**, Finite element analysis of stress driven by creasing within the kirigami structure (PET yield stress, 80 MPa; $E = 31 \text{ kPa}$; skin). **k**, DIC out-of-plane (left) and in-plane (right) strains on a skin phantom during the compressed state of the single-tier transducer ($E = 31 \text{ kPa}$; arrows, direction and magnitude of in-plane deformation). The inner disc rotated 7.5° and translated 0.25 mm vertically relative to the outer ring.



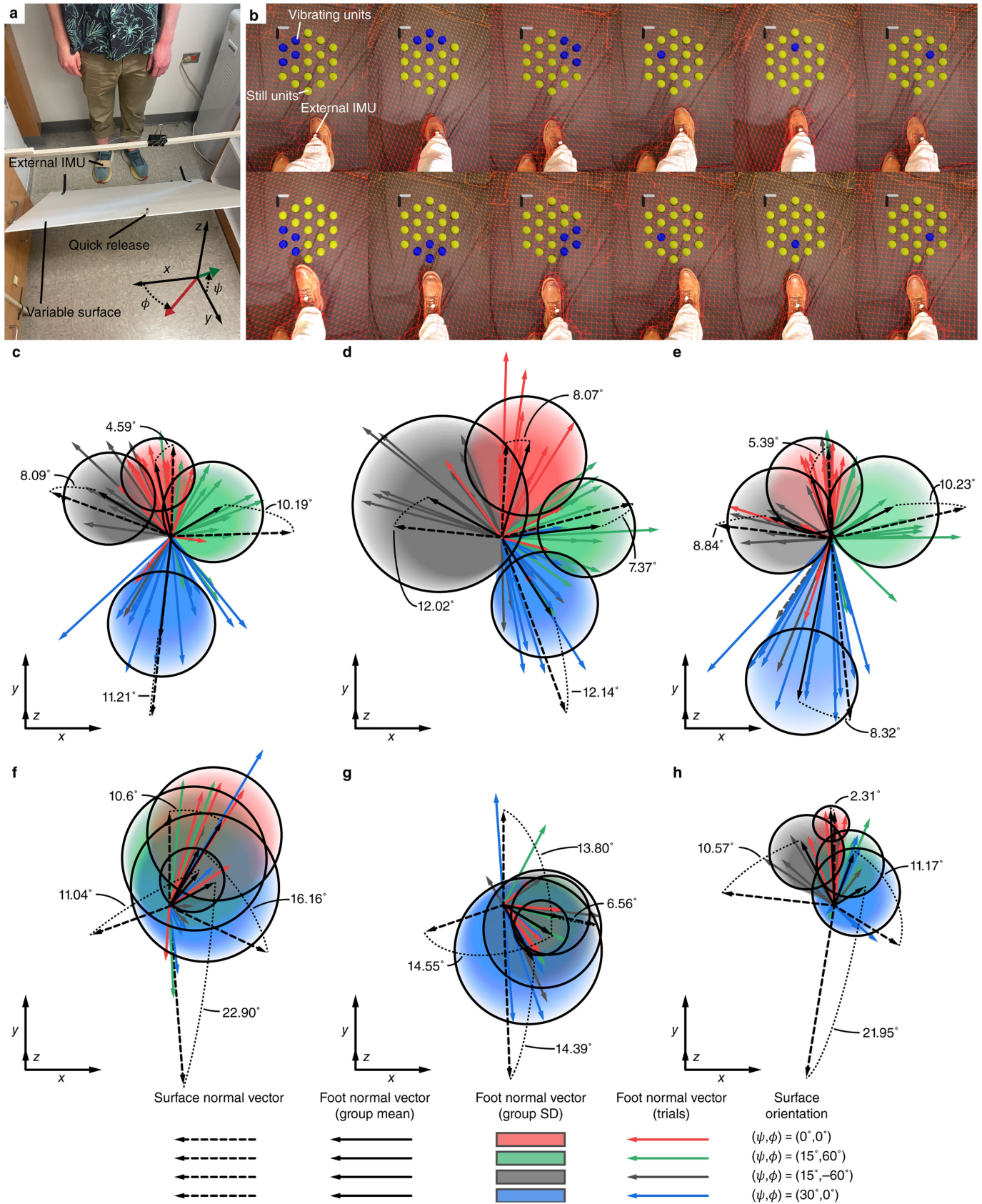
Extended Data Fig. 9 | See next page for caption.

Article

Extended Data Fig. 9 | Visual and balance sensory substitution tasks.

a–h, Visual sensory substitution task. Confusion matrix of participant performance on object identification task ($n = 7$), with the colour map indicating the frequency of occurrence. The P -value was $P = 0.0178$, testing the null hypothesis that selections were made at random between six possible choices (Wilcoxon signed-rank test; $n = 7$). The effect size was large, $r = 0.896$, according to rank-biserial correlation. **a**, Experimental setup of the visual sensory substitution task. **b**, Subject 1, female, age 21 years. **c**, Subject 2, female, age 23 years. **d**, Subject 3, female, age 19 years. **e**, Subject 4, male, age 37 years. **f**, Subject 5, male, age 32 years. **g**, Subject 6, male, age 30 years. **h**, Subject 7, male, age 31 years. **i–s**, Balance sensory substitution task. Participant performance on sharpened Romberg task, measured as the time duration before losing

balance. The P -value across repeated trials and subjects was $P = 0.00103$, testing the null hypothesis that no differences exist in group means. The vertical bars indicate standard deviation, shaded boxes indicate the interquartile range, the horizontal lines above each box indicate medians and filled circles correspond to the means. **i**, Stimulation patterns superimposed on smartphone display during rotation around the forward axis for the balance sensory substitution task. The virtual mesh highlights the LiDAR-reconstructed surface. **j**, Subject 1, female, age 35 years. **k**, Subject 2, female, age 35 years. **l**, Subject 3, female, age 20 years. **m**, Subject 4, female, age 29 years. **n**, Subject 5, female, age 32 years. **o**, Subject 6, male, age 36 years. **p**, Subject 7, male, age 20 years. **q**, Subject 8, male, age 34 years. **r**, Subject 9, male, age 33 years. **s**, Subject 10, male, age 24 years.



Extended Data Fig. 10 | See next page for caption.

Article

Extended Data Fig. 10 | Foot-strike sensory substitution task. Evaluation of the foot-strike sensory substitution system. **a**, Experimental setup depicting reference axes. As part of the task, four separate surfaces were presented at orientations $(\psi, \phi) \in \{(0^\circ, 0^\circ), (15^\circ, 60^\circ), (15^\circ, -60^\circ), (30^\circ, 0^\circ)\}$. **b**, Stimulation patterns superimposed on smartphone display during rotation around the forward axis. The virtual mesh highlights the LiDAR-reconstructed surface. **c–e**, Unit normal vectors of foot and variable surface centred on a common origin during task with feedback. The significance of the results for each individual was evaluated using the Wilcoxon signed-rank test over repeat trials

(across all three phases), given the null hypothesis that the median of the data is identical to the control. Effect size was characterized according to rank-biserial correlation. **c**, Subject 1, male, age 37 years ($n = 57, P < 0.0001, r = -0.59$). **d**, Subject 2, female, age 35 years ($n = 55, P < 0.0001, r = -0.75$). **e**, Subject 3, male, age 21 years ($n = 60, P = 0.00027, r = -0.47$). **f–h**, Unit normal vectors of foot and variable surface centred on a common origin during task without feedback (control). **f**, Subject 1, male, age 37 years. **g**, Subject 2, female, age 35 years. **h**, Subject 3, male, age 21 years.

John A. Rogers, Hanqing Jiang, Yonggang
Corresponding author(s): Huang, Zhaoqian Xie

Last updated by author(s): 8/27/24

Reporting Summary

Nature Portfolio wishes to improve the reproducibility of the work that we publish. This form provides structure for consistency and transparency in reporting. For further information on Nature Portfolio policies, see our [Editorial Policies](#) and the [Editorial Policy Checklist](#).

Statistics

For all statistical analyses, confirm that the following items are present in the figure legend, table legend, main text, or Methods section.

n/a Confirmed

- The exact sample size (n) for each experimental group/condition, given as a discrete number and unit of measurement
- A statement on whether measurements were taken from distinct samples or whether the same sample was measured repeatedly
- The statistical test(s) used AND whether they are one- or two-sided
Only common tests should be described solely by name; describe more complex techniques in the Methods section.
- A description of all covariates tested
- A description of any assumptions or corrections, such as tests of normality and adjustment for multiple comparisons
- A full description of the statistical parameters including central tendency (e.g. means) or other basic estimates (e.g. regression coefficient) AND variation (e.g. standard deviation) or associated estimates of uncertainty (e.g. confidence intervals)
- For null hypothesis testing, the test statistic (e.g. F , t , r) with confidence intervals, effect sizes, degrees of freedom and P value noted
Give P values as exact values whenever suitable.
- For Bayesian analysis, information on the choice of priors and Markov chain Monte Carlo settings
- For hierarchical and complex designs, identification of the appropriate level for tests and full reporting of outcomes
- Estimates of effect sizes (e.g. Cohen's d , Pearson's r), indicating how they were calculated

Our web collection on [statistics for biologists](#) contains articles on many of the points above.

Software and code

Policy information about [availability of computer code](#)

Data collection Ansys, ABAQUS, Labview 2023

Data analysis Matlab 2021b, Origin 2023, R commander

For manuscripts utilizing custom algorithms or software that are central to the research but not yet described in published literature, software must be made available to editors and reviewers. We strongly encourage code deposition in a community repository (e.g. GitHub). See the Nature Portfolio [guidelines for submitting code & software](#) for further information.

Data

Policy information about [availability of data](#)

All manuscripts must include a [data availability statement](#). This statement should provide the following information, where applicable:

- Accession codes, unique identifiers, or web links for publicly available datasets
- A description of any restrictions on data availability
- For clinical datasets or third party data, please ensure that the statement adheres to our [policy](#)

All data generated or analyzed during this study are included in this published article (and its supplementary information files).

Research involving human participants, their data, or biological material

Policy information about studies with [human participants or human data](#). See also policy information about [sex, gender \(identity/presentation\), and sexual orientation](#) and [race, ethnicity and racism](#).

Reporting on sex and gender	Sex of study participants was collected as part of the study, and overall numbers are reported for all experiments throughout the paper and its supplementary information.
Reporting on race, ethnicity, or other socially relevant groupings	Neither race nor ethnicity was considered in this manuscript.
Population characteristics	The ages of individual participants were reported in the paper (ages 19–37).
Recruitment	Healthy normal subjects were recruited randomly from the Northwestern University campus in Evanston, IL, USA and Westlake University campus in Hangzhou, China.
Ethics oversight	Institutional Review Board, Northwestern University (STU00214800); Ethics Committee, Westlake University (20230731JHQ001).

Note that full information on the approval of the study protocol must also be provided in the manuscript.

Field-specific reporting

Please select the one below that is the best fit for your research. If you are not sure, read the appropriate sections before making your selection.

Life sciences Behavioural & social sciences Ecological, evolutionary & environmental sciences

For a reference copy of the document with all sections, see nature.com/documents/nr-reporting-summary-flat.pdf

Life sciences study design

All studies must disclose on these points even when the disclosure is negative.

Sample size	Sample size was not predetermined. Data from 6 participants was collected for mechanical and bistability characterization, 4 participants for adhesion experiments, 12 participants for vibration perception experiments, 12 participants for vibration comparison experiments, 14 participants for torsion perception experiments, 12 participants for torsion array experiments, 15 participants for indentation vs. torsion experiments, 7 participants for the visual sensory substitution task, 10 participants for balance sensory substitution task, and 3 subjects for foot strike sensory substitution task.
Data exclusions	No data was excluded.
Replication	30 transducers were fabricated, and they all performed successfully according to the criteria outlined in the study.
Randomization	Participants were not split into control and experimental groups, and the same conditions were applied across each component of our study.
Blinding	All data was collected in an unbiased manner and experiments was blinded to treatment for final analysis.

Behavioural & social sciences study design

All studies must disclose on these points even when the disclosure is negative.

Study description	Briefly describe the study type including whether data are quantitative, qualitative, or mixed-methods (e.g. qualitative cross-sectional, quantitative experimental, mixed-methods case study).
Research sample	State the research sample (e.g. Harvard university undergraduates, villagers in rural India) and provide relevant demographic information (e.g. age, sex) and indicate whether the sample is representative. Provide a rationale for the study sample chosen. For studies involving existing datasets, please describe the dataset and source.
Sampling strategy	Describe the sampling procedure (e.g. random, snowball, stratified, convenience). Describe the statistical methods that were used to predetermine sample size OR if no sample-size calculation was performed, describe how sample sizes were chosen and provide a rationale for why these sample sizes are sufficient. For qualitative data, please indicate whether data saturation was considered, and what criteria were used to decide that no further sampling was needed.
Data collection	Provide details about the data collection procedure, including the instruments or devices used to record the data (e.g. pen and paper, computer, eye tracker, video or audio equipment) whether anyone was present besides the participant(s) and the researcher, and whether the researcher was blind to experimental condition and/or the study hypothesis during data collection.

Timing	Indicate the start and stop dates of data collection. If there is a gap between collection periods, state the dates for each sample cohort.
Data exclusions	If no data were excluded from the analyses, state so OR if data were excluded, provide the exact number of exclusions and the rationale behind them, indicating whether exclusion criteria were pre-established.
Non-participation	State how many participants dropped out/declined participation and the reason(s) given OR provide response rate OR state that no participants dropped out/declined participation.
Randomization	If participants were not allocated into experimental groups, state so OR describe how participants were allocated to groups, and if allocation was not random, describe how covariates were controlled.

Ecological, evolutionary & environmental sciences study design

All studies must disclose on these points even when the disclosure is negative.

Study description	Briefly describe the study. For quantitative data include treatment factors and interactions, design structure (e.g. factorial, nested, hierarchical), nature and number of experimental units and replicates.
Research sample	Describe the research sample (e.g. a group of tagged <i>Passer domesticus</i> , all <i>Stenocereus thurberi</i> within Organ Pipe Cactus National Monument), and provide a rationale for the sample choice. When relevant, describe the organism taxa, source, sex, age range and any manipulations. State what population the sample is meant to represent when applicable. For studies involving existing datasets, describe the data and its source.
Sampling strategy	Note the sampling procedure. Describe the statistical methods that were used to predetermine sample size OR if no sample-size calculation was performed, describe how sample sizes were chosen and provide a rationale for why these sample sizes are sufficient.
Data collection	Describe the data collection procedure, including who recorded the data and how.
Timing and spatial scale	Indicate the start and stop dates of data collection, noting the frequency and periodicity of sampling and providing a rationale for these choices. If there is a gap between collection periods, state the dates for each sample cohort. Specify the spatial scale from which the data are taken.
Data exclusions	If no data were excluded from the analyses, state so OR if data were excluded, describe the exclusions and the rationale behind them, indicating whether exclusion criteria were pre-established.
Reproducibility	Describe the measures taken to verify the reproducibility of experimental findings. For each experiment, note whether any attempts to repeat the experiment failed OR state that all attempts to repeat the experiment were successful.
Randomization	Describe how samples/organisms/participants were allocated into groups. If allocation was not random, describe how covariates were controlled. If this is not relevant to your study, explain why.
Blinding	Describe the extent of blinding used during data acquisition and analysis. If blinding was not possible, describe why OR explain why blinding was not relevant to your study.

Did the study involve field work? Yes No

Field work, collection and transport

Field conditions	Describe the study conditions for field work, providing relevant parameters (e.g. temperature, rainfall).
Location	State the location of the sampling or experiment, providing relevant parameters (e.g. latitude and longitude, elevation, water depth).
Access & import/export	Describe the efforts you have made to access habitats and to collect and import/export your samples in a responsible manner and in compliance with local, national and international laws, noting any permits that were obtained (give the name of the issuing authority, the date of issue, and any identifying information).
Disturbance	Describe any disturbance caused by the study and how it was minimized.

Reporting for specific materials, systems and methods

We require information from authors about some types of materials, experimental systems and methods used in many studies. Here, indicate whether each material, system or method listed is relevant to your study. If you are not sure if a list item applies to your research, read the appropriate section before selecting a response.

Materials & experimental systems

n/a	Involved in the study
<input checked="" type="checkbox"/>	Antibodies
<input checked="" type="checkbox"/>	Eukaryotic cell lines
<input checked="" type="checkbox"/>	Palaeontology and archaeology
<input checked="" type="checkbox"/>	Animals and other organisms
<input checked="" type="checkbox"/>	Clinical data
<input checked="" type="checkbox"/>	Dual use research of concern
<input checked="" type="checkbox"/>	Plants

Methods

n/a	Involved in the study
<input checked="" type="checkbox"/>	ChIP-seq
<input checked="" type="checkbox"/>	Flow cytometry
<input checked="" type="checkbox"/>	MRI-based neuroimaging

Antibodies

Antibodies used

Describe all antibodies used in the study; as applicable, provide supplier name, catalog number, clone name, and lot number.

Validation

Describe the validation of each primary antibody for the species and application, noting any validation statements on the manufacturer's website, relevant citations, antibody profiles in online databases, or data provided in the manuscript.

Eukaryotic cell lines

Policy information about [cell lines and Sex and Gender in Research](#)

Cell line source(s)

State the source of each cell line used and the sex of all primary cell lines and cells derived from human participants or vertebrate models.

Authentication

Describe the authentication procedures for each cell line used OR declare that none of the cell lines used were authenticated.

Mycoplasma contamination

Confirm that all cell lines tested negative for mycoplasma contamination OR describe the results of the testing for mycoplasma contamination OR declare that the cell lines were not tested for mycoplasma contamination.

Commonly misidentified lines (See [ICLAC](#) register)

Name any commonly misidentified cell lines used in the study and provide a rationale for their use.

Palaeontology and Archaeology

Specimen provenance

Provide provenance information for specimens and describe permits that were obtained for the work (including the name of the issuing authority, the date of issue, and any identifying information). Permits should encompass collection and, where applicable, export.

Specimen deposition

Indicate where the specimens have been deposited to permit free access by other researchers.

Dating methods

If new dates are provided, describe how they were obtained (e.g. collection, storage, sample pretreatment and measurement), where they were obtained (i.e. lab name), the calibration program and the protocol for quality assurance OR state that no new dates are provided.

Tick this box to confirm that the raw and calibrated dates are available in the paper or in Supplementary Information.

Ethics oversight

Identify the organization(s) that approved or provided guidance on the study protocol, OR state that no ethical approval or guidance was required and explain why not.

Note that full information on the approval of the study protocol must also be provided in the manuscript.

Animals and other research organisms

Policy information about [studies involving animals; ARRIVE guidelines](#) recommended for reporting animal research, and [Sex and Gender in Research](#)

Laboratory animals

For laboratory animals, report species, strain and age OR state that the study did not involve laboratory animals.

Wild animals

Provide details on animals observed in or captured in the field; report species and age where possible. Describe how animals were caught and transported and what happened to captive animals after the study (if killed, explain why and describe method; if released, say where and when) OR state that the study did not involve wild animals.

Reporting on sex

Indicate if findings apply to only one sex; describe whether sex was considered in study design, methods used for assigning sex. Provide data disaggregated for sex where this information has been collected in the source data as appropriate; provide overall

numbers in this Reporting Summary. Please state if this information has not been collected. Report sex-based analyses where performed, justify reasons for lack of sex-based analysis.

Field-collected samples

For laboratory work with field-collected samples, describe all relevant parameters such as housing, maintenance, temperature, photoperiod and end-of-experiment protocol OR state that the study did not involve samples collected from the field.

Ethics oversight

Identify the organization(s) that approved or provided guidance on the study protocol, OR state that no ethical approval or guidance was required and explain why not.

Note that full information on the approval of the study protocol must also be provided in the manuscript.

Clinical data

Policy information about [clinical studies](#)

All manuscripts should comply with the ICMJE [guidelines for publication of clinical research](#) and a completed [CONSORT checklist](#) must be included with all submissions.

Clinical trial registration

Provide the trial registration number from ClinicalTrials.gov or an equivalent agency.

Study protocol

Note where the full trial protocol can be accessed OR if not available, explain why.

Data collection

Describe the settings and locales of data collection, noting the time periods of recruitment and data collection.

Outcomes

Describe how you pre-defined primary and secondary outcome measures and how you assessed these measures.

Dual use research of concern

Policy information about [dual use research of concern](#)

Hazards

Could the accidental, deliberate or reckless misuse of agents or technologies generated in the work, or the application of information presented in the manuscript, pose a threat to:

No	Yes
<input type="checkbox"/>	<input type="checkbox"/> Public health
<input type="checkbox"/>	<input type="checkbox"/> National security
<input type="checkbox"/>	<input type="checkbox"/> Crops and/or livestock
<input type="checkbox"/>	<input type="checkbox"/> Ecosystems
<input type="checkbox"/>	<input type="checkbox"/> Any other significant area

Experiments of concern

Does the work involve any of these experiments of concern:

No	Yes
<input type="checkbox"/>	<input type="checkbox"/> Demonstrate how to render a vaccine ineffective
<input type="checkbox"/>	<input type="checkbox"/> Confer resistance to therapeutically useful antibiotics or antiviral agents
<input type="checkbox"/>	<input type="checkbox"/> Enhance the virulence of a pathogen or render a nonpathogen virulent
<input type="checkbox"/>	<input type="checkbox"/> Increase transmissibility of a pathogen
<input type="checkbox"/>	<input type="checkbox"/> Alter the host range of a pathogen
<input type="checkbox"/>	<input type="checkbox"/> Enable evasion of diagnostic/detection modalities
<input type="checkbox"/>	<input type="checkbox"/> Enable the weaponization of a biological agent or toxin
<input type="checkbox"/>	<input type="checkbox"/> Any other potentially harmful combination of experiments and agents

Plants

Seed stocks

Report on the source of all seed stocks or other plant material used. If applicable, state the seed stock centre and catalogue number. If plant specimens were collected from the field, describe the collection location, date and sampling procedures.

Novel plant genotypes

Describe the methods by which all novel plant genotypes were produced. This includes those generated by transgenic approaches, gene editing, chemical/radiation-based mutagenesis and hybridization. For transgenic lines, describe the transformation method, the number of independent lines analyzed and the generation upon which experiments were performed. For gene-edited lines, describe the editor used, the endogenous sequence targeted for editing, the targeting guide RNA sequence (if applicable) and how the editor was applied.

Authentication

Describe any authentication procedures for each seed stock used or novel genotype generated. Describe any experiments used to assess the effect of a mutation and, where applicable, how potential secondary effects (e.g. second site T-DNA insertions, mosaicism, off-target gene editing) were examined.

ChIP-seq

Data deposition

- Confirm that both raw and final processed data have been deposited in a public database such as [GEO](#).
- Confirm that you have deposited or provided access to graph files (e.g. BED files) for the called peaks.

Data access links

May remain private before publication.

For "Initial submission" or "Revised version" documents, provide reviewer access links. For your "Final submission" document, provide a link to the deposited data.

Files in database submission

Provide a list of all files available in the database submission.

Genome browser session (e.g. [UCSC](#))

Provide a link to an anonymized genome browser session for "Initial submission" and "Revised version" documents only, to enable peer review. Write "no longer applicable" for "Final submission" documents.

Methodology

Replicates

Describe the experimental replicates, specifying number, type and replicate agreement.

Sequencing depth

Describe the sequencing depth for each experiment, providing the total number of reads, uniquely mapped reads, length of reads and whether they were paired- or single-end.

Antibodies

Describe the antibodies used for the ChIP-seq experiments; as applicable, provide supplier name, catalog number, clone name, and lot number.

Peak calling parameters

Specify the command line program and parameters used for read mapping and peak calling, including the ChIP, control and index files used.

Data quality

Describe the methods used to ensure data quality in full detail, including how many peaks are at FDR 5% and above 5-fold enrichment.

Software

Describe the software used to collect and analyze the ChIP-seq data. For custom code that has been deposited into a community repository, provide accession details.

Flow Cytometry

Plots

Confirm that:

- The axis labels state the marker and fluorochrome used (e.g. CD4-FITC).
- The axis scales are clearly visible. Include numbers along axes only for bottom left plot of group (a 'group' is an analysis of identical markers).
- All plots are contour plots with outliers or pseudocolor plots.
- A numerical value for number of cells or percentage (with statistics) is provided.

Methodology

Sample preparation

Describe the sample preparation, detailing the biological source of the cells and any tissue processing steps used.

Instrument

Identify the instrument used for data collection, specifying make and model number.

Software

Describe the software used to collect and analyze the flow cytometry data. For custom code that has been deposited into a community repository, provide accession details.

Cell population abundance	<i>Describe the abundance of the relevant cell populations within post-sort fractions, providing details on the purity of the samples and how it was determined.</i>
Gating strategy	<i>Describe the gating strategy used for all relevant experiments, specifying the preliminary FSC/SSC gates of the starting cell population, indicating where boundaries between "positive" and "negative" staining cell populations are defined.</i>

Tick this box to confirm that a figure exemplifying the gating strategy is provided in the Supplementary Information.

Magnetic resonance imaging

Experimental design

Design type	<i>Indicate task or resting state; event-related or block design.</i>
Design specifications	<i>Specify the number of blocks, trials or experimental units per session and/or subject, and specify the length of each trial or block (if trials are blocked) and interval between trials.</i>
Behavioral performance measures	<i>State number and/or type of variables recorded (e.g. correct button press, response time) and what statistics were used to establish that the subjects were performing the task as expected (e.g. mean, range, and/or standard deviation across subjects).</i>

Acquisition

Imaging type(s)	<i>Specify: functional, structural, diffusion, perfusion.</i>
Field strength	<i>Specify in Tesla</i>
Sequence & imaging parameters	<i>Specify the pulse sequence type (gradient echo, spin echo, etc.), imaging type (EPI, spiral, etc.), field of view, matrix size, slice thickness, orientation and TE/TR/flip angle.</i>
Area of acquisition	<i>State whether a whole brain scan was used OR define the area of acquisition, describing how the region was determined.</i>
Diffusion MRI	<input type="checkbox"/> Used <input type="checkbox"/> Not used

Preprocessing

Preprocessing software	<i>Provide detail on software version and revision number and on specific parameters (model/functions, brain extraction, segmentation, smoothing kernel size, etc.).</i>
Normalization	<i>If data were normalized/standardized, describe the approach(es): specify linear or non-linear and define image types used for transformation OR indicate that data were not normalized and explain rationale for lack of normalization.</i>
Normalization template	<i>Describe the template used for normalization/transformation, specifying subject space or group standardized space (e.g. original Talairach, MNI305, ICBM152) OR indicate that the data were not normalized.</i>
Noise and artifact removal	<i>Describe your procedure(s) for artifact and structured noise removal, specifying motion parameters, tissue signals and physiological signals (heart rate, respiration).</i>
Volume censoring	<i>Define your software and/or method and criteria for volume censoring, and state the extent of such censoring.</i>

Statistical modeling & inference

Model type and settings	<i>Specify type (mass univariate, multivariate, RSA, predictive, etc.) and describe essential details of the model at the first and second levels (e.g. fixed, random or mixed effects; drift or auto-correlation).</i>
Effect(s) tested	<i>Define precise effect in terms of the task or stimulus conditions instead of psychological concepts and indicate whether ANOVA or factorial designs were used.</i>
Specify type of analysis:	<input type="checkbox"/> Whole brain <input type="checkbox"/> ROI-based <input type="checkbox"/> Both
Statistic type for inference	<i>Specify voxel-wise or cluster-wise and report all relevant parameters for cluster-wise methods.</i>
(See Eklund et al. 2016)	
Correction	<i>Describe the type of correction and how it is obtained for multiple comparisons (e.g. FWE, FDR, permutation or Monte Carlo).</i>

Models & analysis

n/a	Involved in the study
	<input type="checkbox"/> Functional and/or effective connectivity
	<input type="checkbox"/> Graph analysis
	<input type="checkbox"/> Multivariate modeling or predictive analysis
Functional and/or effective connectivity	<i>Report the measures of dependence used and the model details (e.g. Pearson correlation, partial correlation, mutual information).</i>
Graph analysis	<i>Report the dependent variable and connectivity measure, specifying weighted graph or binarized graph, subject- or group-level, and the global and/or node summaries used (e.g. clustering coefficient, efficiency, etc.).</i>
Multivariate modeling and predictive analysis	<i>Specify independent variables, features extraction and dimension reduction, model, training and evaluation metrics.</i>